ELECTROSYNTHESS AND CHARACTERIZATION OF IRON OXIDE NANO-COMPOSITE SUPERPARAMAGNETIC THIN FILMS

ELECTROSYNTHESIS AND CHARACTERIZATION OF IRON OXIDE NANO-COMPOSITE SUPERPARAGNETIC THIN FILMS

By

Shane Turcott, B.Eng.

A Thesis

Submitted to the School of Graduate Studies

In Partial Fulfillment of the Requirements

For the Degree of:

Masters of Applied Science

McMaster University

MASTER OF APPLIED SCIENCE
(Materials Science and Engineering)

McMaster University
Hamilton, Ontario

TITLE : Electrosynthess and Characterization of Iron Oxide Nano-Composite Superparamagnetic Thin Films

AUTHOR : Shane R. Turcott, B.Eng. (McMaster University)

SUPERVISORS : Dr. I. Zhitomirsky
Dr. M. Niewczas

NUMBER OF PAGES : xi, 104

ABSTRACT

Using a newly developed method of co-electrodeposition, superparamagnetic films containing iron oxide nano-particles in a polymer matrix have been fabricationed. The method is based upon the electrosynthesis of inorganic particles dispersed within a polymer matrix obtained by electrophoretic deposition. The results showed the prepared materials to exhibit superparmagnetic properties at room temperature. The influence of the deposition conditions and the electrolyte composition on the magnetic properties of the film have been studied. Adjusting the polymer content within the electrolyte has been shown to control the iron oxide to polymer composition ratio in the deposited film. This significantly affects the particle size, inter-particle distance and magnetic properties of the material. TGA analysis was used to determine the iron oxide to polymer composition ratio. The morphology of the films was studied by SEM and AFM techniques. Two theoretical approaches have been used to calculate the particle size in the developed films and the results are in good agreement with TEM observations. Saturation magnetization ranged up to 19.71 emu/g at room temperature in the films obtained. The blocking temperatures have been determined from the results of DC and AC measurements, the latter performed from 10 to 10,000Hz. Blocking temperatures varied with film composition but remained below 111°K. These results set the framework for discussion of the structure and magnetic properties of nano-materials synthesized using this fabrication method.

ACKNOWLEDGEMENTS

I would like to sincerely thank both Dr. Igor Zhitomirsky and Dr. Marek Niewczas for their guidance, support, patience and knowledge over the past two years. Not only have they directed this research to success, they have made this into a great learning for myself. I am very honoured to have had their supervision.

Thanks to Dr. Anthony Petric for his contribution as my initial supervisor and his advice throughout.

People whose technical assistance was much appreciated are Andy Duft, Jim Garret, Chris Butcher, Wenhe Gong, Frank Gibbs, Steve Koprich, Ed McCaffery, Doug Culley and Mike Palme.

The financial support of MMO and McMaster University is gratefully acknowledged.

Finally, I'd like to thank the people who made the past two years more than just a learning experience but also a growing experience: my friends. A special mention to Boris Martin, Jean Duquette and Ayesha Ahmed as through them I have learned as much about life as I have in science these past two years.

> "Live as if you were to die tomorrow,
> Learn as if you were to live forever."
> -*Gandhi.*

TABLE OF CONTENTS

LIST OF TABLES

LIST OF FIGURES

CHAPTER 1

LITERATURE REVIEW

1.1 Fundamentals of Magnetic Materials

For a more detailed review of traditional magnetics, please refer to Brown, Kittel, Smith and Callister, (Brown,1962; Kittel 1949; Smith, 1993; Callister, 2003).

1.1.1 Origin of Magnetism

Magnetization is the result of uncancelled magnetic moment created by electron motion. The most fundamental magnetic moment is created by the spin of one electron producing 9.27 x 10^{-24} Am^2 called the "Bohr Magnetron", μ_B. Electron orbital motion also creates a magnetic moment of $m_l\mu_B$ where m_l is the quantum number of the electron.

The net dipole of an atom is the summation of the magnetic moments produced by its electrons by spin and orbital motion. Arrangement of electron motion within an atom leads to partial, and sometimes complete, cancellation of magnetic moment. Paired electrons, due to the Pauli Exclusion Principle, have anti-parallel spins and summation of the spin magnetic moment for paired electrons is zero. Filled electron states (in its natural state) have balanced electron orbital motion and complete cancellation of orbital magnetic moment. Therefore, intrinsic atomic magnetic dipoles are the result of magnetic moments originating from 1) spin motion of unpaired, localized electrons and 2) the orbital motion of partially filled electron states.

From this principle, several types of magnetism exist including diamagnetism, paramagnetism, anti-ferromagnetism, ferromagnetism, ferrimagnetism and, in very specific cases, superparamagnetism. All materials exhibit at least one of these types of magnetic behaviour.

1.1.2 Magnetic Properties

The magnetic interaction between the material and an externally applied magnetic field is of great engineering interest. The internal field strength within a material is called the "magnetic induction" or "flux density", denoted as B. The externally created magnetic field from the material is called the *intensity of magnetization*, often referred to as just *magnetization*, and is denoted as M. Under an applied field, H, the magnetic induction can be defined as per equation 1.1.

$$B = H + 4\pi M \tag{1.1}$$

Materials with high magnetization, such as ferromagnetic and some ferrimagnetic materials, the magnetization term can be much greater than the applied field contribution. In such cases the simplification of $B \approx \mu_0 M$ can appropriately be used.

The magnetization of a material is proportional to the applied field. M*agnetic susceptibility*, X, is described by equation 1.2.

$$X = \frac{M}{H} \tag{1.2}$$

1.2 Diamagnetism and Paramagnetism

1.2.1 Diamagnetism

The presence of an externally applied field slightly offsets the orbital motion of the electrons preventing complete cancellation of orbital magnetic moment in filled electron states. This leads to the creation of an extremely small magnetic induction in the opposite direction to the magnetic field. This effect is called *diamagnetism* and the magnetic susceptibility ranges in the order of -10^{-6} (negative due to opposite direction to field). Due to the negative magnetic susceptibility, diamagnetic materials are weakly repulsed from high magnetic fields.

All materials possess diamagnetic behaviour but, as it is so weak, such behaviour can only be observed when all other forms of magnetism are absent. Diamagnetic materials are considered non-magnetic as they only show magnetic properties when in the presence of an externally applied magnetic field.

1.2.2 Paramagnetism

For materials in which atoms have incomplete magnetic cancellation from electron spin and/or electron orbital motion, each atom has a magnetic dipole causing the atom to act as a small, permanent magnetic. In paramagnetic materials, no interaction between neighboring atomic dipoles occurs and the orientation of each atomic dipole is random, creating a macroscopic net magnetization of zero. In the presence of an externally applied magnetic field, the atomic dipoles align in the direction of the applied field, creating a small magnetic effect. Magnetic susceptibilities of paramagnetic materials range between 10^{-5} to 10^{-2}. Once the applied field is removed, thermal agitation randomizes the atomic dipoles to eliminate the materials magnetization.

Paramagnetic materials, like diamagnetic, are categorized as non-magnetic because no magnetism remains without the presence of an external magnetic field.

1.3 Ferromagnetism, Ferrimagnetism and Anti-Ferromagnetism

Certain transition and rare-earth elements exhibit the ability to possess permanent, large magnetic moments in the absence of an external field. The large magnetic moments are the result of unpaired, uncancelled electron spin moments. Transition and rare-earth elements follow an irregular filling sequence with regard to the 3rd and 4th orbital quantum states. One of the associated phenomena is that electrons in these quantum states show a strong tendency for unpaired electrons to occupy the same spin orientation according to Hund's 1st Rule. This results in spin alignment of all unpaired electrons within the valence band, leading to significant magnetic fields. Although there is orbital magnetic moment present, its contribution is comparatively small and can be safely disregarded.

To minimize overall magnetic energy, such materials exhibit *spontaneous magnetization* as the atomic magnetic dipoles demonstrate macroscopic ordering. Providing a positive exchange interaction, atomic magnetic dipoles are aligned in macroscopic regions known as *domains*.

Metallic materials with this magnetic behaviour are categorized as *ferromagnetic* and materials such as iron, cobalt and nickel are of great engineering importance. Magnetic susceptibilities in ferromagnetic materials range up to the order of 10^6.

Ferrimagnetic materials show similar macroscopic magnetic behaviour to ferromagnetic but from a different microscopic mechanism. In such materials, atomic dipoles are arranged anti-parallel but due to either differences in magnetic dipole strength or the ratio of anti-parallel magnetic dipoles, a net magnetic moment is produced.

In the case of a negative exchange interaction between atomic dipoles, neighboring atoms are arranged anti-parallel in magnetic orientation causing complete cancellation between atomic magnetic dipoles. Such behaviour is known as *anti-ferromagnetism* as the net magnetization of the material is zero.

1.4 Magnetic Energies

The magnetic configuration within a bulk material is organized to minimize the overall magnetic energy. In the theoretical case of a perfect, single ferrimagnetic crystal with no defects, the three magnetic energies (with relevance to this work) can be summed together to give the overall magnetic energy as per equation 1.3.

$$E_{mag} = E_K + E_w + E_m \tag{1.3}$$

where E_{mag} is the total magnetic energy, E_K is the anisotropy energy, E_W is the energy arising from domain walls and E_M is the energy associated with the magnetic field, called "magnetostatic energy". The stable configuration can be found as the minimum total magnetic energy.

In the case of a pure, single crystal with all the magnetic dipoles aligned in one direction (single domain), the large external field is created and the material has a high magnetostatic energy. This case is schematically illustrated in Fig 1.1a. The arrangement of two oppositely oriented domains, shown Fig 1.1b, reduces both the magnetic field and the magnetostatic energy by half, lowering the total magnetic energy of the system.

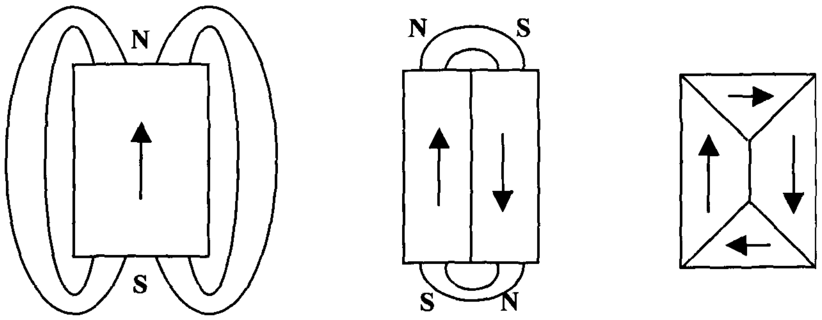

Figure 1.1 (a) showing a single domain crystal, (b) multi-domained crystal, and (c) a multi-domained crystal with *domains of closure.*

Continually creating more domains would reduce the magnetostatic energy in an inverse proportional relationship. However, each newly created domain creates a new interface between the domains. These domain interfaces are called "*Bloch Walls*" and have their own energy contribution which must be considered. Subdivision into more domains can be expected to continue until the reduction in magnetostatic energy is less than the energy associated with the increased Bloch wall energy.

Another possible domain arrangement enabling further reduction in total magnetic energy is the incorporation of *domains of closure*, shown in Figure 1.1c. In this arrangement, the magnetization direction is always normal to the material surface and no magnetic poles are formed. The magnetic flux is completed within the material with no external magnetic field, making the magnetostatic energy negligible.

1.4.1 Exchange Energy

Exchange Energy accounts for the interactions between atomic dipoles and is minimized when all dipoles are aligned. Deviation in magnetic direction between two atoms increases the exchange energy, increasing with misalignment. Exchange energy is dependent only upon the angle between spins of other atoms and independent of crystal structure. Spontaneous magnetization of domains is energetically favourable to reduce exchange energy.

1.4.2 Anisotropy Energy

The energy required to magnetize a lattice in a specific direction differs along different crystallographic directions. The lowest energy directions are used as a reference energy level conveniently set at zero called the "directions of easy magnetization" and, in the absence of external fields, domains are naturally oriented along these directions. To change the direction of magnetization from this easy direction to a hard direction requires excess energy, most often significant amounts of excess energy. This energy is called *"anisotropy energy"* or, specific to crystalline influences, *"magnetocrystalline anisotropy"*.

Magnetocrystalline anisotropy arises from spin-orbit-crystalline field interactions. The spin interacts with the orbital motion and the orbital motion interacts with the inhomogeneous electric field of the crystal structure. Thus different crystallographic planes, having specific electric fields, will have spins influenced by the appropriate orbital motion. This creates different levels of energy required to align the electron's spin in specific crystallographic directions as these factors must be included.

Magnetocrystalline energy, in a simple, uniaxial model can be described as equation 1.4.

$$E_K = KV \sin^2\theta \qquad (1.4)$$

where K is the uniaxial anisotropy energy per unit volume, V is the particle volume and θ is the angle between the magnetic moment and the easy axis direction.

A second form of anisotropy comes from the influence of the shape of the domain called "shape anisotropy". In the case of a bulk polycrystalline material with no preferred grain texture, the crystal has no net anisotropy due to the randomness of the preferred directions. However, in the case of materials which have a preferred grain orientation and shape (as in the case of cold worked materials), or the shape of the material itself influences the domain shape, a shape anisotropy is observed. In well designed materials, this shape anisotropy can dominate the anisotropy terms. As the coercive force is proportional to the anisotropy energy, this phenomenon is of considerable interest in areas of high coercive magnet development.

1.4.3 Domain (Bloch) Walls

The Bloch Wall was given its name after F. Bloch who was one of the first to study the transition between domains. His contribution was showing the transition between the spin directions of two domains being a gradual shift in spin directions over many atomic planes. This transition is governed by the balance between exchange energy and anisotropy energy.

In order to minimize the exchange energy, the spin orientation transition takes place over a large number of atomic planes. Exchange energy associated with the bloch wall is inversely proportional to the number of atomic layers to which the transition occurs. The wall thickness is limited by the anisotropy as the spin orientations must rotate between directions of easy magnetization through directions of high anisotropy. The Bloch Wall Energy is described by equation 1.5.

$$E_w = A\sigma_w = A(\sigma_{ex} + \sigma_{anis}) = A\left[2\pi\left(\frac{JKA^2}{a}\right)^{1/2} + KNa\right] \qquad (1.5)$$

where A is the bloch wall area, σ_w is the wall energy per unit area, σ_{ex} is the exchange energy per unit area, σ_{anis} is the anisotropy per unit area, J is the exchange integral, N is the number of atomic planes the transition occurs over and 'a' is the lattice constant. A typical 180° wall thickness in iron is approximately 100 nm. Domains of closure boundaries are a 90° rotation leading to thinner walls with lower energy.

1.4.4 Magnetostatic Energy

Magnetostatic Energy, also known as "Magnetic Field Energy", is the energy used to create magnetic poles on the surface of the material. These magnetic poles in turn create the magnetic field for which ferro/ferrimagnetics are so well known for. The magnetostatic energy is described by equation 1.6.

$$E_m = -\frac{1}{2}\int (H \bullet M)dV \tag{1.6}$$

1.5 Magnetization Behaviour of Ferro/Ferrimagnetic Material

It has already been discussed that the domain structure is configured to minimize the total magnetic energy in its natural state. By the addition of an externally applied field, the total magnetic energy is changed and the domain structure is changed. The energy from the applied field is added to the magnetic energy as shown in equation 1.7.

$$E_{mag} + M_s VH\cos\theta = E_K + E_W + E_M \tag{1.7}$$

where M_s is the saturation magnetization of the material and θ is the angle between the applied field and axis of easy magnetization.

By subjecting an applied field to a ferro/ferrimagnetic material, the net magnetization of the material is increased. This increase is due to two separate mechanisms. The first mechanism to typically occur is the preferrential growth of domains which share alignment to the magnetic field. This growth is at the expense of domains which are oriented against the field and is schematically shown in Figure 1.2. This domain growth has two stages which are separated into (1) reversible boundary displacement and (2) irreversible boundary displacement. Boundary displacement can occur until it has consumed the entire crystal.

The second mechanism to increase the net magnetization is the rotation of the domain's magnetic orientation (shown in Figure 1.2d). This mechanism usually occurs after boundary displacement as it requires high magnetic fields to overcome the anisotropy energy in order to orient the spin direction away from the directions of easy magnetization.

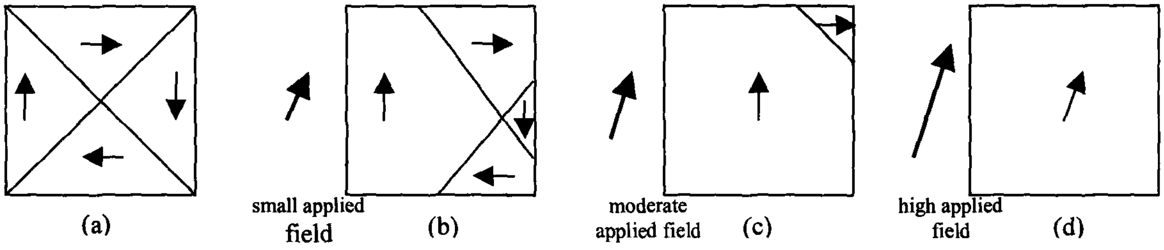

Figure 1.2 (a) Material with spontaneous domain structure. (b) Reversible boundary displacement occurring at small applied field. Domains in favourable orientation of field grow at expense of non-favourably oriented domains. (c) Irreversible boundary displacement as domains non-favourably oriented become eliminated from moderate applied field. (d) Rotation of domain's magnetic orientation at high applied fields.

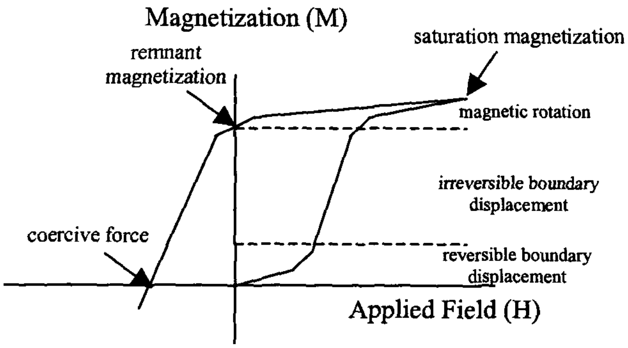

Figure 1.3 Initial virgin curve and demagnetization to a typical hysteresis magnetic material plotted on applied field versus magnetization. The three phases of magnetization are shown.

Upon completion of maximum allowable boundary displacement when the domains have oriented in the direction of the magnetic field, maximum magnetization is achieved and it is called "saturation magnetization" denoted as M_s. The *virgin curve* to a ferro/ferrimagnetic material is shown in Figure 1.3.

Removal of the applied field from a magnetized material only partially de-magnetizes the material and a *remnant magnetization* is retained. Without the applied field, the domains re-orient themselves along directions of easy magnetization, reducing the anisotropy energy and causing some reduction in net magnetization. Magnetization is retained due to the irreversible boundary displacements which had occurred during magnetization as domains are oriented favourably with past magnetizing field. Spontaneous creation of domains oriented in other directions, including the energy to create and move bloch walls, requires large amounts of energy. Without excess energy, the material retains the large domains oriented in the directon of the historically applied field.

The *coercive force* is the applied field (oriented in the opposite direction of the previously applied field) required to demagnetize the material. The coercive field supplies energy for bloch wall movement, creation of new bloch walls and re-orientation of existing domains. This is an important engineering property to magnetic materials and is often referred to as the material's *coercivity*.

The typical hysteresis loop from a complete magnetic cycle through an applied field, reverse field and back to an applied field is shown in Figure 1.4.

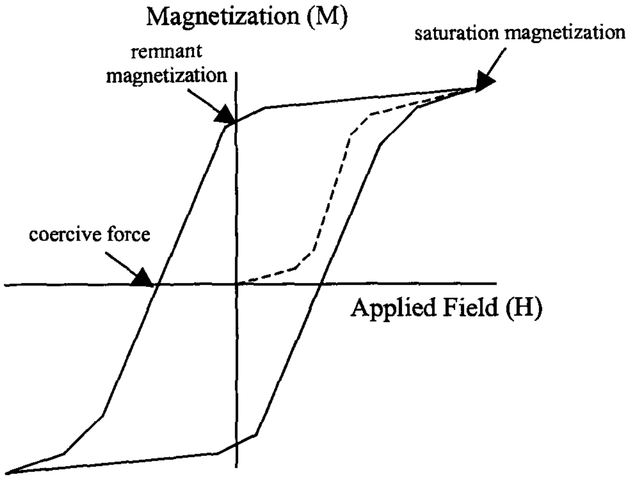

Figure 1.4 Hysteresis loop of a ferro/ferrimagnetic material.

1.6 Nanoparticles and Superparamagnetism

The previous section described magnetization in bulk materials where the magnetic properties are dominated by the volume related magnetic energies of anisotropy and magnetostatic energy. As the size of a material is decreased to below the order of 100 nm, changes in the magnetic behaviour are observed as the interface energies and surface effects becomes more important than volume magnetic energies.

1.6.1 Single Domain Particles

At a critical size, in the order of 100 nm, the reduction in magnetostatic energy by the arrangement of two or more domains will be less than the energy associated with the bloch wall required for the interface between domains. At this condition, the particle having only one domain is energetically favourable and the particle is termed "single domain" (Néel, 1955; Kittel, 1946, Leslie-Pelecky, 1996).

Single domain particles, although still technically ferro/ferrimagnetic, exhibit different magnetic relaxation compared to bulk materials. Magnetization and demagnetization no longer occurs by boundary displacement. Magnetization behaviour in single domain particles is based solely upon the magnetization rotation of each domain, each particle. As this rotation occurs from the easy magnetization direction to another direction, large amounts of energy are needed to overcome the anisotropy energy barrier for relaxation. This results in large increases in the coercive force of small particle assemblies and small particle materials have been engineered to have coercive forces several times larger than the bulk material.

The coercive force must overcome the anisotropy energy needed to move the direction of magnetization through hard directions in order to eliminate the effects of previous magnetization. Magnetocrystalline anisotropy energy and shape anisotropy are the two predominate forms of anisotropy involved. Shape anisotropy in particular can create significant increases in the coercive force. Deviation from spherical geometry of the particle by an aspect ratio of 1.1 to 1.5 can create coercive forces four times that in bulk material. An aspect ratio of 5 can double the coercive force again (Leslie-Pelecky, 1996).

1.6.2 Superparamagnetism

Decreasing the size of the particles even further into the order of only a few nanometers, the coercive force drops from large values down to zero. As the anisotropy energy is proportional to volume ($E_K \propto KV$), at such small particle sizes the thermal energy of the particle is comparable to, if not larger than, the anisotropy energy. Since the magnetic reversal energy barrier at such particle sizes is approximately equal to the anisotropy energy, the magnetic moment of each particle may be rotated by thermal fluctuation preventing the material from having stable magnetization (Dormann, 1997).

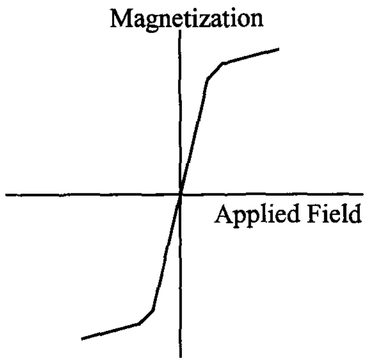

Figure 1.5 Characteristic superparamagnetic behaviour under an applied field

Figure 1.5 shows a magnetization versus applied field plot typical of a material consisting of an assembly of superparamagnetic particles. Under an applied field, each particle's magnetic orientation is rotated to align with the field, creating a net magnetization. The anisotropy energy, being the primary energy barrier to magnetization (and demagnetization), is extremely small and the particles align at low applied fields. The effect of this is seen as the material reaches its saturation magnetization at weak applied fields as compared to the bulk materials which have high anisotropy and require domain wall movement. The net magnetization of the assembly of small particles nears that of the bulk material and can have a similar, but lower, saturation magnetization.

Upon removal of the applied field, the thermal energy quickly randomizes each particle's orientation, creating an average magnetic moment of zero.

1.6.3 Blocking Temperature

The loss of magnetization upon removal of the applied field is due to the thermal energy overcoming the magnetic reversal energy barrier (Dormann, 1997). Below a critical temperature not enough thermal energy will be available to thermally equilibrate and randomize each particle's magnetic orientation. This transition temperature is called the "blocking temperature", denoted as T_B, and below it, the material shows a remanent magnetization and coercive force (Figure 1.6). This blocking temperature is crucial in the study of superparamagnetic nano-particles.

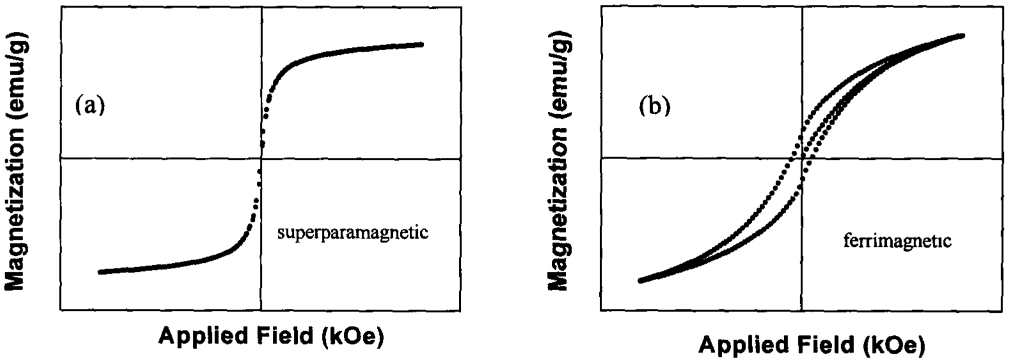

Figure 1.6 (a) above the blocking temperature, superaparamagnetic behaviour, (b) below the blocking temperature showing a hystersis curve including remnant magnetization.

Blocking temperature is a function of measurement time and applied field. The blocking temperature decreases with the field strength and time allowed to demagnetize. Therefore the obtained blocking temperature is dependent upon the experimental measuring conditions used. Blocking temperature is also dependent upon particle size. As all fabrication methods currently used create particles within a size distribution, the blocking temperature itself is usually measured as an average over all particle sizes.

1.6.4 Relaxation

Relaxation time, τ (in sec), is the time required for an assembly of particles to reach thermodynamic equilibrium. According to the Néel model (Néel, 1955), relaxation is described as per equation 1.8.

$$\tau = \tau_0 \exp\left(\frac{E_{rev}}{kT}\right) \tag{1.8}$$

where τ_0 is the standard relaxation constant, E_{rev} is the magnetic reversal energy barrier, k is the Boltzman constant and T is the absolute temperature. It should be noted that τ_0 is often treated as constant but actually depends on the applied field, particle size, anisotropy constant and temperature (Kneller, 1966; Dormann, 1997). The Néel model assumes a random orientation of easy axis directions in the particle assembly, uniaxial symmetry and that the magnetic orientation is mainly along the direction of easy magnetization. A system is considered in thermodynamic equilibrium when $t >> \tau$.

In the absence of a magnetic field and for a thermally equilibrated system ($T >> T_B$), the probability of individual particles changing magnetic orientation to another direction of easy magnetization is $1/2\tau$ per unit of time. In a uniaxial assembly with N particles and P particles oriented in the Oz magnetic direction, the change in P is given by equation 1.9 (Dormann, 1997).

$$dP = \frac{(N-P)}{2\tau}dt - \frac{P}{2\tau}dt \tag{1.9}$$

The addition of an applied field in the Oz direction causes the decrease of the energy along the Oz direction, as per equation 1.10.

$$E_{mag,Oz} = KV\sin^2\theta - HM_{nr}V\cos\theta \tag{1.10}$$

where M_{nr} is the non-relaxing magnetization of the particle. As the magnetization along the Oz direction is below that of the Oz' direction, the inequality between energy minima leads to variation between magnetic reversals. τ^+ is the magnetic reversal time to switch from the lowest minima to higher minima (from the Oz direction to the Oz' direction) and τ^- is the magnetic reversal time to change orientation from the higher to lower minima. Equation 1.9 now can be written as equation 1.11.

$$dP = \frac{(N-P)}{2\tau^-}dt - \frac{P}{2\tau^+}dt \tag{1.11}$$

and relaxation time is described by equation 1.12.

$$\frac{1}{\tau} = \frac{1}{\tau^+} + \frac{1}{\tau^-} \tag{1.12}$$

When the applied field is removed, Oz and Oz' become equal, τ^+ and τ^- become equal and therefore can be described by equation 1.13.

$$\tau^{+} = \tau^{-} = 2\tau \qquad (1.13)$$

Upon removal of the applied field, complete randomization of the magnetic orientations of the particle assembly in order to achieve demagnetization takes τ length of time.

1.6.5 Particle Size

The thermal energy is fixed at a given temperature. Therefore, for any specific temperature there is a critical upper limit in particle size, above which the anisotropy barrier is larger than the available thermal energy and the particle will behave ferrimagnetically. The magnetocrystalline anisotropy energy, and thus the approximate magnetic reversal energy barrier, was described earlier in equation 1.2 as: $E_K = KV\sin^2\theta$. Therefore the maximum anisotropy energy possible is at θ=90°, making $E_{Kmax} = KV$. Setting this equal to the thermal energy, the critical radius of the particle, R_c, can be approximated by equation 1.14.

$$R_c = \left(\frac{3kT}{4\pi K}\right)^{1/3} \qquad (1.14)$$

Typical values for superparamagnetic particle sizes at room temperature are of the order of 10 nm. In the case of a limited relaxation time, the critical particle size decreases.

As well as an upper dimension to the particle size for superparamagnetic behaviour, there exists a lower dimensional limit for the particle size to obtain superparamangetic properties. The magnetic properties of the atoms near the surface of the particle are strongly modified. This is often called the 'magnetic dead zone' but more accurately, the atoms still have magnetic properties, just significantly modified (Dormann, 1997). This layer's thickness depends on the material and particle size but ranges between 5 to 10 Å (Chantrell, 1978, Kim 2001; Prene, 1993; Dormman, 1996). The magnetically dead skin, which at nano-sized particles can be a significant portion of the magnetic material, explaining the lower saturation magnetization of nano-particles compared to the bulk material. As particle size decreases, a larger volume fraction of the magnetic material is near the surface with magnetically altered properties. Therefore, the saturation magnetization is reduced with the reduction in particle size.

1.6.6 Particle-Particle Interaction

Each of the individual nano-particles are permanent magnets and only when the magnetic moment of each particle in an assembly is randomized will the net magnetic moment equal zero. The simplest situation is that each particle acts independently with regards to the thermal fluctuation of the magnetic moment and this case is seen in composite materials containing a low density of magnetic material. Magnetic reversal energy barriers are specific to each particle. In the case of composite materials with a high density of magnetic material and relatively small particle distancing, the magnetic behaviour of individual particles can be influenced by the magnetostatic field of neighboring particles. This phenomenon is called "particle-particle interaction", or "interparticle interaction", and can affect the magnetic behaviour of the particle assembly. High interparticle interaction prevents particles from acting individually and magnetic reversal depends upon particles acting as a collective state.

The particle interactions depend upon a $1/d^3$ relation where d is the distance between particles. The magnetic properties of the matrix can greatly influence the particle interaction. In the case of a magnetically insulating matrix, via superexchange interactions (depending of particle/matrix bonding), interactions can extend to long distances.

1.7 Experimental Characterization of Superparamagnetic Properties

1.7.1 Magnetization under Applied Fields

The most traditional magnetic characterization technique is measuring the magnetization under an applied field. A sample is subjected to an increasing applied field while magnetization is continuously measured. At the maximum applied field (H_{max}), magnetization is decreased to the reverse field strength ($-H_{max}$) and then increased back to the maximum applied field (H_{max}).

Figure 1.5 displays the characteristic superparamagnetic magnetization under an applied field. Above the blocking temperature, non-hysteresis behaviour occurs as no remanent magnetization or coercive force is observed. Saturation magnetization can be determined by extrapolating the linear region of magnetization obtained at high fields. The extrapolated magnetization at the H=0 axis is the saturation magnetization, M_S.

Superparamagnetic behaviour will show superimposition of magnetization when plotted against the applied field normalized by the temperature (while above the blocking temperature).

1.7.2 Zero-Field-Cooled and Field Cooled Magnetization

During Zero-Field-Cooled (ZFC) magnetic measurements, the sample is cooled to near absolute zero, a magnetic field is applied and the magnetization is measured as the temperature is raised to the maximum temperature, usually around room temperature. At very low temperatures, magnetization of the particles is blocked. Increasing the temperature will show an increase in M_{ZFC} until a maximum M_{ZFC} is obtained corresponding to the average blocking temperature, $T_{B\ avg}$. Continuous increase in temperature will decrease the M_{ZFC}. At temperatures above the *breaking temperature*, T_{bra} (the blocking temperature of the largest particles within the particle size distribution) the material shows thermodynamic equilibrium properties. Without significant interparticle interactions, magnetization follows the Curie-Weiss law given in equation 1.15.

$$\chi = \frac{C}{T - \Theta_{SP}} \tag{1.15}$$

where $C=VM_s^2T/3k$ and Θ_{SP} is the superparmagnetic temperature constant.

Field-Cooling (FC) measurements are similar to ZFC but cooling is done under an applied field. Magnetization measurements are taken when the temperature is being increased while the sample is under an applied field. ZFC and FC curves overlap when the material is superparamagnetic and thermally equilibrated. The temperature at which the ZFC and FC deviate corresponds to the breaking temperature, T_{bra}. Figure 7 displays a schematic of a ZFC and FC plot.

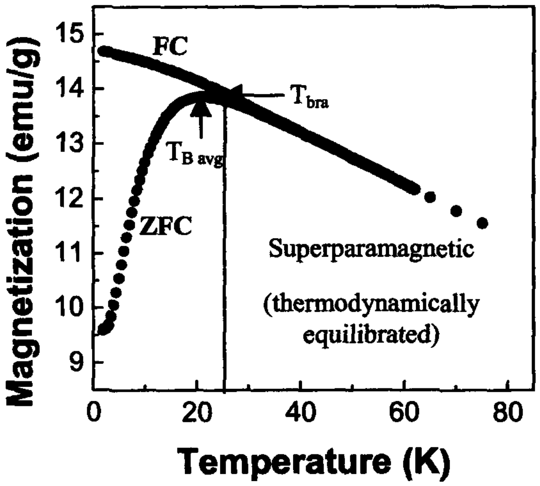

Figure 1.7 ZFC and FC example curve showing schematically blocking temperature, $T_{B\,avg}$ and breaking temperature, T_{bra}.

1.7.3 AC Susceptibility

AC susceptibility measurements subject the sample to an alternating magnetic field and the magnetization is measured between applied fields. Relaxation can be studied as a function of time (the inverse to frequency).

Figure 1.8 shows a plot of the real component to AC susceptibility (χ') versus temperature with typical superparamagnetic characteristics. At very low temperatures insufficient thermal energy exists to randomize the magnetic orientation of the particles in the provided time. As temperature increases, the susceptibility increases until a maximum value is obtained at T_{max}. T_{max} corresponds to the transition temperature between the blocked state and relaxed state (superparamagnetic). Therefore T_{max} is the average blocking temperature specific to a given frequency. Above T_{max} the susceptibility decreases with temperature as per the Curie-Weiss Law (equation 1.15) (Brown, 1962). Data from AC susceptibility measurements can be fitted into the Néel model (equation 1.8) to obtain the magnetic reversal energy barrier.

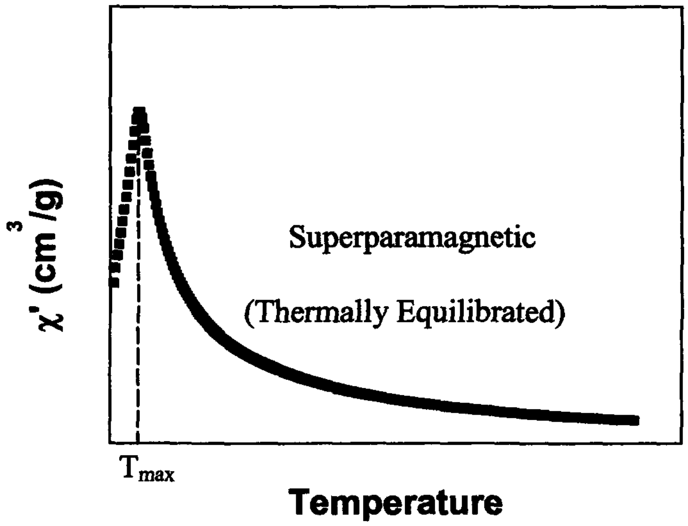

Figure 1.8 Real component of AC susceptibility curve.

1,8 Iron Oxide

1.8.1 Crystal Structure

Magnetite (Fe_3O_4) is an inverse spinel made up of an oxygen fcc structure (Cornell, 1996; Valenzuela, 1994; Standley, 1972). One-eight of the tetrahedral sites and one-half of the octahedral interstitial sites are filled with iron cations (designated A and B sites respectively). As the divalent iron cation has a larger radius than the trivalent cation, an inverse spinel structure is preferred to locate the divalent cation at the smaller of the interstitial sites. Therefore the divalent iron cation is located at the octahedral site with trivalent iron cations filling the tetrahedral (A site) and remaining octahedral sites (B sites). Using the notation of $(A)[B_2]O_4$ to describe cation location, magnetite is described as $(Fe^{3+})[\ Fe^{2+}Fe^{3+}]O_4$. One unit cell contains 32 oxygen, 8 ferric cations at the tetrahedral sites, 8 ferrous cations at half the octahedral sites and 8 ferric cations occupying the remaining octahedral sites. Figure 1.9 shows the crystal structure of magnetite.

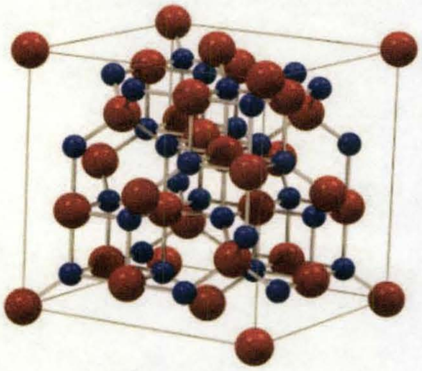

Figure 1. 9 Illustration of magnetite crystal structure. Red spheres represent oxygen anions, blue spheres represent iron cations. (Callister, 2003)

The tetrahedral and octahedral sites are stacked along the [111] plane. To accommodate interstitial occupancy and size difference between iron cations with different oxidation states, the oxygen atoms are slightly shifted from the center of symmetry. The unit cell length is a=0.839 nm. At 120°K, the cubic structure shifts to a monoclinic unit cell and is called the Verwey transition (Iida, 1982). Below this transition temperature, magnetite losses its near metallic conductivity.

Maghemite (γ-Fe_2O_3) has a similar but defective structure to magnetite. Unlike magnetite, all of the iron cations are in the trivalent state and cation vacancies compensate to maintain charge neutrality for the unit cell. The unit cell contains 32 oxygen anions, 21 $^1/_3$ trivalent iron cations and 2 $^2/_3$ vacancies. The vacancies are randomly distributed within the octahedral sites. The lattice parameter is a=0.834nm but can increase up to 0.839nm (that of magnetite) as divalent iron cations are introduced. Maghemite and magnetite often exist together in solid solution.

1.8.2 Bulk Magnetic Properties

Each trivalent iron cation, Fe^{3+}, with five unpaired electrons in the d orbitals, produces a magnetic moment of 5.9 Bohr magnetons (Valenzuela, 1994). The divalent iron cation, Fe^{2+}, has an experimentally measured magnetic moment ranging from 5.1 to 5.5 Bohr magnetons. The oxygen anion, O^{2-}, is magnetically neutral due to completely filled shells.

In the magnetite structure, the iron cations are too far apart for direct exchange. The separation by oxygen anions leads to indirect exchange, a phenomenon known as *superexchange.* Oxygen p orbital electrons, from ionic bonding with the iron, show partial occupation of the empty iron 3d states. Due to the Pauli Exclusion principle, the occupying electron will have an anti-parallel orientation to the iron cation unpaired electrons and the second oxygen p orbital and when bonded with another cation, will force the second cation to have oppositely oriented electron spin. As the p orbitals are linear, the strongest superexchange is found at 180° and is weakest at 90°.

The A-O-B angle between Fe^{3+} cations at the tetrahedral and octahedral sites is 127° leading to a dominating A-O-B superexchange over the 90° B-O-B angle between octahedral sites. This causes an anti-parallel arrangement between the octahedral and tetrahedral Fe^{3+} cations, causing complete cancellation of the trivalent iron cations. Therefore, the magnetic properties of magnetite are solely from the magnetic contribution of the Fe^{2+} cations.

Magnetite exhibits a saturation magnetization between 80 to 100 emu/g at room temperature (Cornell, 1996). It has a Curie temperature of 858 K. Magnetite has an anisotropy constant in the order of 10^4 to 10^5 erg/cm^3 with the easy direction of magnetization along the [111] plane.

Maghemite has very similar magnetic behaviour to magnetite. Eight of the 13 $^1/_3$ octahedral Fe^{3+} cancel out the eight anti-parallel tetrahedral Fe^{3+}. The magnetic properties of maghemite are therefore from the remaining 5 $^1/_3$ octahedral cations. Maghemite has a saturation magnetization between 60 and 80 emu/g, a higher Curie temperature of 950 K and an anisotropy constant in the range of 10^5 erg/cm^3.

Saturation magnetization of magnetite, maghemite and other oxides are summarized in Table 1.1.

Table 1.1 Saturation magnetization of bulk iron oxides (Cornell, 1996)

Iron Oxide Chemical Formula	**Iron Oxide Name**	**Saturation Magnetization at 300 K (emu/g)**
Fe3O4	Magnetite	80 - 100
γ-F_2O_3	Maghemite	60 – 80
α- F_2O_3	Haematite	0.3
FeO	Wustite	Anti-ferromagnetic
δ-FeOOH		7 - 20

1.9 Experimental Properties of Iron Oxide, Nano-Composite, Superparamgnetic Materials

Several studies have been conducted on nano-composite, iron oxide materials with interest in magnetic properties. Unfortunately, what few studies do exist, are extremely different in terms of fabrication method, matrix material, particle size/distribution, magnetic material density/arrangement and analysis techniques. This prevents direct comparison between various studies and no comprehensive understanding of the topic yet exists.

The most directly relevant study was performed by Zhitomirksy (Zhitomirsky, 2003). Zhitomirsky used the same co-electrodeposition process as this research and iron oxide nano-composite deposits were prepared with 0.5 and 1.0 g/L poly(diallyldimethylammonium chloride) [PDDA] solution concentrations. Deposits showed superparamagnetic behaviour. ZFC and FC measurements showed the deposit made with 0.5 g/L PDDA solution concentration to have a blocking temperature of 25°K.

Prené (Prené,1993) studied the magnetic effects of interacting and non-interacting nano-particles by ZFC and FC measurements. Prené prepared γ-Fe_2O_3 nano-particles in an aqueous medium by a solution chemical method. Samples were categorized as 'C' or 'C/50', both having similar particle size but C/50 having an oxide to polymer mass ratio 1/50 that of C. The average particle spacing was 1.5<D> and 6<D> for C and C/50 respectively with <D> being the mean particle diameter. ZFC and FC measurements of C, C/50 and a sample where particles were allowed to flocculate are shown in Figure 1.10. Prené observed a weak increase in M_{FC} for samples C at temperatures below the maximum M_{ZFC} temperature and associated this magnetic saturation due to increased interparticle interaction when compared with sample C/50. Prené showed a narrower magnetic reversal energy barrier distribution with an increase in interparticle interaction. ZFC and FC magnetization deviated from Curie-Weiss behaviour with an increase in interparticle interaction.

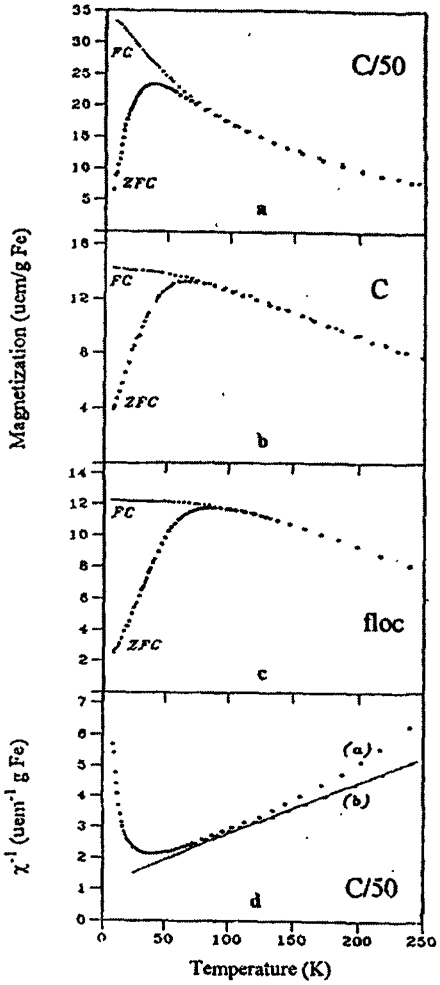

Figure 1.10 ZFC and FC measurements of (a) C/50, (b) C, (c) floculated particles. (d) Inverse susceptibility for C and C/50 (Prené 1993)

Kim *et al* (Kim, 2001) formed magnetite particles by alkalinizing a ferric and ferrous chloride salt solution with sodium hydroxide under a nitrogen environment.

Particles were coated with sodium oleate by a chemical solution process. Calculated particle size ranged from 1.3 to 6 nm and particle size was dependent upon solution pH and sodium hydroxide concentration. TEM measurements showed an extra 1.2 nm in diameter over the calculated particle size of 6 nm. Differences between TEM and calculated particle size explained as the magnetically dead layer, indicating the layer thickness was 0.6 nm. The highest saturation magnetization obtained was 42.1 emu/g at 300 K. Blocking temperature, determined by ZFC and FC measurements (using a field of 10 Oe) was 150 K for samples with a calculated particle size of 6 nm. The standard relaxation constant, using the Néel model from AC susceptibility measurements, was calculated as $\tau_0 = 7.8 \times 10^{-24}$ seconds.

Work done by Kroll (Kroll, 1996) using a sol-gel fabrication method was successful in creating nano magnetite particles within an alginate. Particle size was between 3 to 6 nm in diameter and TEM images showed a low volumetric density with particles distributed unevenly. Saturation magnetization ranged up to 23.27 emu/g at room temperature.

Chantrell *et al* (Chantrell, 1978) studied magnetite nano-particles in ferrofluid suspensions of diester, water, petroleum and cobalt/tolunene. Table 1.2 lists the obtained saturation magnetization, calculated particle size and TEM measurement of particle size values. Note that saturation magnetization was calculated differently by extrapolating magnetization versus 1/applied field. Saturation magnetization was the extrapolated magnetization at the 1/H=0 axis. Differences between calculated particle diameter and

TEM observations were associated with the magnetic dead zone near the surface of the particle.

Table 1.2 Saturation magnetization and particle size results from Chantell *et al* (Chantrell, 1978)

Matrix Fluid	Saturation Magnetization (emu/cm^3)	Calculated Particle Diameter (nm)	TEM Particle Diameter (nm)
Diester	15.92	11	14
Water	8.76	12	20.5
Petroleum	3.98	7.5	90
Cobalt/Toluene	7.17	4.7	75

Later work done by Chantrell along with El-Hilo and O'Grady (El-Hilo, 1992), studied the particle interaction of magnetite ferrofluids using ZFC and FC measurements. Particle sizes were observed and calculated as being 10 and 7.8 nm respectively. The anisotropy constant was calculated as $K=4.4 \times 10^5$ erg/cm^3 from experimental results which are consistent with the past study conducted be Tari *et al* (Tari, 1980). Blocking temperature was shown to increase with an increase in saturation magnetization by a power law: $T_B \propto M_s^m$. Although consistent with other experimental results, the increase in blocking temperature contradicts the Néel theory (Neel 1949) which explained particle interaction as another field which behaves as a externally applied field on the system. Chantrell has done computer and mathematical modeling of low field susceptibility magnetization of fine particle assemblies (Chantrell, 1983; 1985).

Dormann has conducted a series of studies, with various counterparts, on interparticle interactions of γ-Fe_2O_3 (Dormann, 1996, 1997, 1998). Using AC susceptibility measurements, Dormann has repeatedly shown an increase in both the blocking temperature and magnetic reversal energy barrier with either a decrease in particle-particle distancing and/or increase in nearest-neighbors. Interparticle interaction caused deviation of the Néel theory (Néel, 1949). Although still empirically valid, obtained τ_0 values were well below physical values. Figure 1.11 shows Sample IF (center-to-center particle distancing of 21 nm), with low interparticle interaction, fitting well into the Néel theory with an appropriate τ_0 value. Samples IN and Floc (7.3 and 6.8 nm center-to-center particle distancing respectively) to have τ_0 values well below physical values. Samples were found to have an average diameter of 4.7 nm.

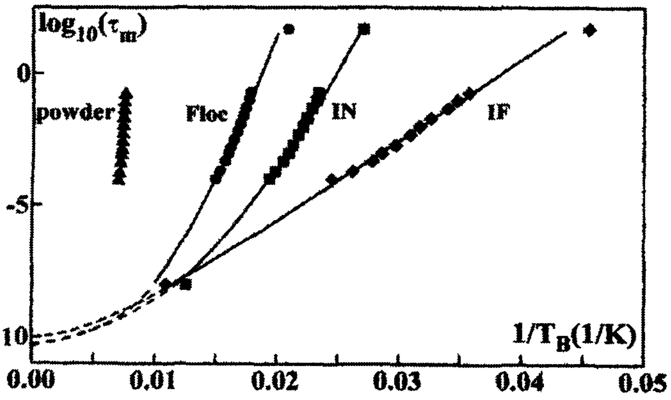

Figure 1.11 Relaxation time versus 1/temperature from Dormann (Dorman, 1996).

It was also shown by Dormann that the observed anisotropy barrier of the particles (K=3.9 x 10^5 erg/cm^3) was an order of magnitude higher than the bulk magnetocrystalline anisotropy of maghemite (K_{bulk}=4.6 x 10^4 erg/cm^3). He hypothesized the higher observed anisotropy was from surface anisotropy contributions of the nano-particles.

CHAPTER 2

RESEARCH OBJECTIVE

The purpose of this work was to study both the fabrication of iron oxide/polymer nano-composite thin films by a co-electrodeposition process and the superparamagnetic properties of these deposited films. The primary research focused upon the effects of solution concentration of poly(diallydimethylammonium chloride) and its relation to the magnetic properties of the final deposit. Nano-composite films were fabricated using five different polymer solution concentrations and two different experimental procedures. Deposited films were characterized using thermogravimetic analysis, electron microscopy, atomic force microscopy, X-ray diffraction and magnetic measurements. Magnetic measurements consisted of magnetization under low and high applied fields, zero-field-cooling, field-cooling and AC susceptibility measurements. The relation of solution polymer concentration during co-electrodeposition upon the deposited film's composition, iron oxide phase, nano-particle size and ultimately the magnetic properties was studied.

CHAPTER 3

EXPERIMENTAL PROCEDURE

A series of composite films composed of iron oxide nano-particles and various polymer matrices were fabricated through electrochemical deposition. Work done included the development of deposition equipment, selection of polymer matrix, modification of deposition parameters and comprehensive characterization of the magnetic properties of the developed films. In the next section details of the synthesis and characterization of these films are described.

3.1 Materials

The following chemical reagents were used in the electrochemical deposition of nano-composite iron oxide films:

Deionized water		
Ferric chloride hexahydrate	$(FeCl_3\cdot 6H_2O)$	Aldrich
Ferrous chloride tetrahydrate	$(FeCl_2\cdot 4H_2O)$	Aldrich
Forming Gas	(7% H_2, balance N_2)	Vital Air
Polyethylenimine (80% ethoxylated) [PEI] -(M_w of 70 000 g/mol)		Aldrich
poly(acrylamide-co-diallylmethylammonium chloride) [PAM-PDDA]		Aldrich
Poly(diallyldimethylammonium chloride) [PDDA] -(M_w of 400 000 to 500 000 g/mol) -(M_w of 100 000 to 200 000 g/mol)		Aldrich
Reagent Grade Methanol		Caledon

3.2 Substrates

The following substrate materials were used in the electrochemical deposition of nano-composite iron oxide films:

Copper
Platinum
Graphite

Platinum was used as the anode material for all experiments. The anodes were of 25 x 50 x 0.1mm in dimension.

Copper cathodes were cut to 10 x 50 x 1mm dimensions. The substrate was mechanically polished on one side. Polishing steps included grinding at 120 and 220 grit followed by polishing at 9, 6, 3 and 1μm using diamond suspensions. The final stage was a 0.05 μm polish using colloidal silica.

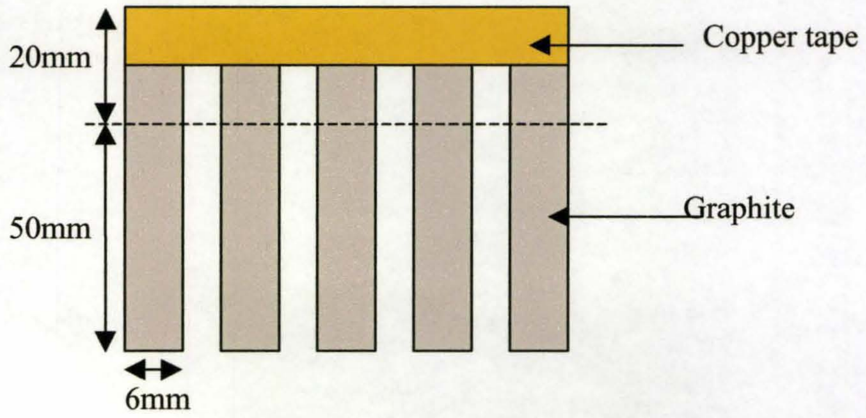

Figure 3.1 Diagram of graphite cathode

Platinum cathodes were used at both 25 x 50 x 0.1mm and 50 x 50 x 0.1mm dimensions. Platinum cathodes were cleaned by submersion in a hydrogen peroxide, nitric acid and deionized water solution of equal parts.

Graphite cathodes were polished using 120, 220, 500 and 1000 grit paper. The graphite plates were 70 x 6 x 2 mm in dimension. Five graphite cathodes were used in parallel, held together with copper tape, arranged with a 5 mm spacing (as shown in Figure 3.1). 5 cm of the cathode was submerged into the solution during deposition.

3.3 Equipment

The deposition equipment used to test and to compare new polymers for use as the polymer matrix was a fabricated *electrode holder* using a 300 ml beaker. The platinum anodes were suspended into the solution 2 cm on either side of the cathode. 270 ml electrolyte solution was used per deposition. Deposition with this apparatus was done using an open (air) environment.

Deposition in a reducing environment was performed using a *deposition vessel* designed and constructed specifically for these experiments. The apparatus was a sealed glass vessel with gas input and output at the bottom and top of the vessel respectively. The gas output was connected to a bubbler. A valve at the bottom of the vessel allows for the solution to be drained at controlled rates, preventing a compromise in the gas environment. A glass cup, denoted the 'spoon', was used to add ingredients to the solution after being sealed within the vessel. Platinum anodes were suspended parallel on either side of the cathode with a 2.2 cm spacing. 1800 ml of electrolyte solution was used per deposition. The deposition vessel sat upon a magnetic stirring plate. Figure 3.2

shows the power supply, the deposition vessel sitting on a magnetic stirring plate and the bubbler used.

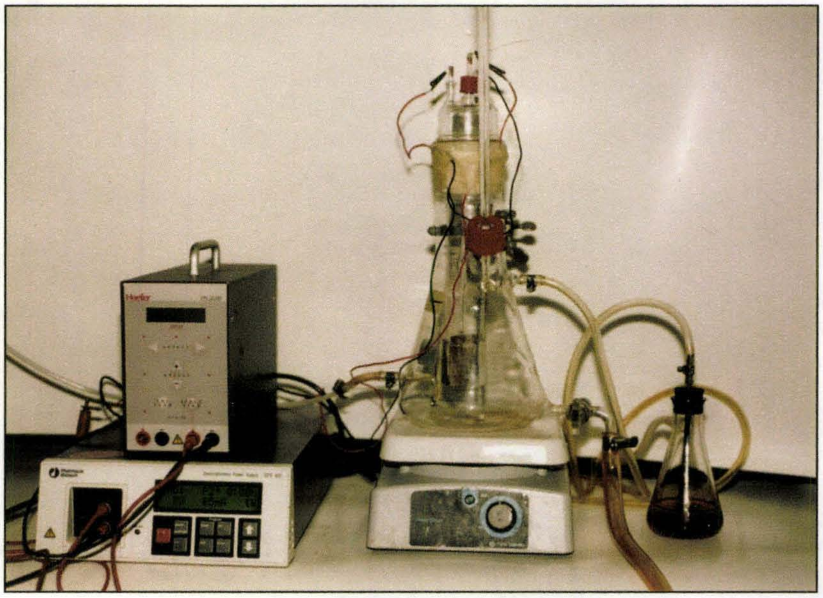

Figure 3.2 Deposition vessel.

3.4 Solutions and Deposition Conditions

3.4.1 Deposition of Nano-Composite Film using PEI Polymer Matrix

Electrolyte stock solution was based upon a 950 ml methanol, 50 ml deionized water solution, 0.9 g of ferric chloride hexahydrate and 0.33 g of ferrous chloride tetrahydrate were added to make the total iron ion concentration of 5 mmol/l with a Fe^{3+}:Fe^{2+} molar ratio of 2:1. Polymer concentrations and deposition currents are listed in Table 3.1. Deposition was done in an air environment.

Table 3.1 Experimental conditions for the deposition of nano-composites based upon PEI as the matrix

Sample	Polymer Concnetration (g/L)	Deposition Current (mA/cm2)
PEI-1	0.4	1
PEI-2	0.4	3
PEI-3	0.4	5
PEI-4	0.8	1
PEI-5	0.8	3
PEI-6	0.8	5

3.4.2 Deposition of Nano-Composite Film using PAM-PDDA Polymer Matrix

The deposition of the films containing PAM-PDDA as the matrix material were conducted using different methanol:water ratios as listed in Table 3.2. 0.9 g of ferric chloride hexahydrate and 0.33 g of ferrous chloride tetrahydrate were added to make the iron ion concentration of 5 mmol/l. Deposition current density was 4 mA/cm^2 for three minutes in an air environment.

Table 3.2 Experimental conditions for the deposition of nano-composites based upon PAM-PDDA matrix

Sample	Methanol (%)	Water (%)	Polymer (g/L)
PAM-1	50	50	0.5
PAM-2	75	25	0.5
PAM-3	90	10	0.5
PAM-4	90	10	1.0

3.4.3 Deposition of Nano-Composite Film using PDDA Polymer Matrix

0.9 g/L of ferric chloride hexahydrate salt was added to 50 ml of de-ionized water within deposition vessel and allowed to dissolve under moderate stirring conditions. The assigned weight of PDDA (M_w = 400,000 to 500,000 g/mol unless otherwise stated) was added and with another 50 ml of de-ionized water. 1700 ml of methanol was added slowly. 0.33 g of the ferrous chloride tetrahydrate salt was placed on the 'spoon' and inserted into the vessel making sure the spoon (and salt) were well above the electrolyte level. The vessel was sealed and forming gas was flushed through the vessel at a moderate rate for a minimum of 30 minutes. Following, the spoon was lowered into the electrolyte and given 10 minutes to allow the ferrous chloride salt to dissolve into solution.

Stirring was halted 3 minutes before deposition. Deposition time ranged from three to five minutes limited only by adhesion. Following deposition, the cathode was raised out from the electrolyte solution and solution drained at a slow rate to maintain bubbling within the bubbler. The drying phase was a 24 hour period at room temperature with constant gas flow.

Table 3.3 lists the experimental parameters used for each experiment including solution polymer concentration, cathode material and current density. Samples made under these conditions are categorized as 'P1 Series' and denoted sample identification begins with 'P1'.

The Second Series of experiments using PDDA had the same experimental procedure at the First Series with two improvements: 1) enhanced gas flow throughout the experiment and 2) improved drying conditions. Table 3.4 lists the experimental conditions used for the "P2 Series", denoted beginning with 'P2'.

Table 3.3 Experimental conditions for the deposition of nano-composites based upon PDDA matrix, P1 Series

Sample	Polymer (g/L)	Cathode Material	Current Density (mA/cm2)	Comments
P1-1	0	Platinum	10	
P1-2	0.4	Platinum	10	
P1-3	0.6	Platinum	10	
P1-4	0.8	Platinum	10	
P1-5	1.2	Platinum	10	
P1-6	0	Platinum	10	
P1-7	0.4	Platinum	10	
P1-8	0.6	Platinum	10	
P1-9	0.8	Platinum	10	
P1-10	1.2	Platinum	10	
P1-11	0.6	Copper	3	-deposition time: 2 minutes
P1-12	0.6	Graphite	10	
P1-13	0.8	Graphite	10	
P1-14	0	Platinum	10	
P1-15	0.4	Platinum	10	
P1-16	0.4	Platinum	10	-used PDDA of M_w = 100,000 to 200,000
P1-17	0.4	Platinum	10	
P1-18	0.4	Platinum	10	-deposited in air environment
P1-19	0.8	Platinum	10	
P1-20	1.2	Platinum	10	-stirring during deposition
P1-21	0.4	Copper	3	
P1-22	0.4	Copper	3	-deposition time: 5 minutes
P1-23	1.2	Copper	3	-deposition time: 5 minutes

Table 3.4 Experimental conditions for the deposition of nano-composites based upon PDDA matrix, P2 Series

Sample	Polymer (g/L)	Cathode Material	Current Density (mA/cm2)	Comments
P2-1	0	Platinum	10	
P2-2	0.4	Platinum	10	
P2-3	0.6	Platinum	10	
P2-4	0.8	Platinum	10	
P2-5	0.6	Platinum	10	
P2-6	0.6	Platinum	10	
P2-7	0.6	Platinum	10	
P2-8	0.6	Platinum	10	
P2-9	0.6	Platinum	10	
P2-10	0.6	Platinum	10	
P2-11	0.6	Platinum	10	-methanol chilled in ice water
P2-12	0.6	Platinum	10	-methanol chilled in ice water (18°C)
P2-13	0.6	Platinum	5	-methanol chilled in ice water (19°C)
P2-14	0.6	Platinum	10	
P2-15	0.6	Platinum	10	
P2-16	0.8	Platinum	10	
P2-17	0.8	Platinum	10	
P2-18	0.8	Platinum	10	
P2-19	0.8	Platinum	10	
P2-20	0.8	Platinum	10	

3.5 Thermogravimetric Analysis

Thermogravimetric analysis (TGA) was done using a Netzsch STH-409 thermoanalyzer. Samples P1-6, P1-7, P1-8 , P1-9 , P1-10 , P2-5 and P2-6 were studied using TGA. A minimum of 10 mg of sample material was evaluated. Samples were heated to 1200 C at a rate of 5 C/min in an air environment. Alumina crucibles were used.

3.6 Scanning Electron Microscopy

SEM samples were studied using a Philips 515 scanning electron microscope (SEM). Graphite cathodes (with deposited film) were submerged in liquid nitrogen and fractured. For observing film cross-sections, the fractured surface was mounted upwards. Between cross-section and surface-on views, for each deposited sample approximately 20 sections were mounted to be observed at various magnifications.

3.7 Atomic Force Microscopy

AFM samples were cut to a 1 x 1 cm dimension and the topography was obtained by tapping mode, AFM measurements using a NanoScopeIIIa Digital Instruments Multimode Scanning Probe Microscope.

3.8 X-Ray Diffraction

X-ray diffraction was done using monochromatized Cu K_α radiation on a Nicolet 12 diffractometer. A scanning speed of 0.5 °/minute was used for Samples P1-14 and P1-15 in a range of diffracting angles 2θ from 10 to 90°. Sample P2-7 was evaluated at a scanning speed of 0.33 °/minute from 20 to 80°.

3.9 Magnetic Properties

Samples P1-1 through P1-5 and P2-1 through P2-4 were evaluated for their magnetic properties. Deposited films were mechanically removed from the cathode and used for magnetic measurements. A minimum of 0.0150 g were used for magnetic measurements.

Magnetic properties were studied using a PPMS-9, Quantum Design System. The magnetization of the films were studied under an applied field at temperatures ranging from 2 to 298 K. The P1 Series were tested at both low and high applied fields. Low field magnetic measurements exposed the material, starting at a zero field, to an applied field increasing incrementally to 10 kOe, followed by decreasing to –10 kOe and then cycling back to 10 kOe. High field measurements were conducted using the same procedure but ranging in field strength of ±90 kOe. The magnetic properties of the P2 series were also evaluated at high field strengths of ±90 kOe.

Magnetic susceptibility was studied at frequencies ranging from 10 to 10 000 Hz with an AC excitation field with an amplitude of 4 Oe. The retained magnetization of the material was measured after half the cycle time was completed. Measurements were conducted at temperatures between 2 and 298 K.

Zero Field Cooling (ZFC) and Field Cooling (FC) measurements were performed under the external field of 200 and 500 Oe, from 2 to 298 K with a heating rate of 0.5 K/minute. ZFC measurements were conducted by cooling the sample to 2 K in the absence of a field, and measuring the magnetization as the sample was heated up to 298 K in an applied field. FC measurements were taken by cooling the sample down to 2 K while under an applied field and measuring the magnetization of the material temperatures were increased to 298 K, still under an applied field.

CHAPTER 4

RESULTS

4.1 Deposition of Nano-Composite Films using PEI Polymer Matrix

Samples PEI-2 and PEI-3, deposited with 0.4 g/L PEI solution concentration using 3 and 5 mA/cm^2 current densities respectively, showed inadequate adhesion. Samples made with 0.8 g/L PEI concentrations (PEI-4, PEI-5 and PEI-6) showed acceptable adhesion at all current densities. Samples PEI-4, PEI-5 and PEI-6 exhibited low magnetization.

4.2 Deposition of Nano-Composite Films using PAM-PDDA Polymer Matrix

Addition of PAM-PDDA to either methanol or a water/methanol solution caused the polymer to react. PAM-PDDA/water/methanol solution was successfully prepared by adding the polymer to water followed by the slow addition of methanol.

Inadequate film adhesion was observed at all water/methanol mixtures used. Sample PAM-1 showed large accumulation of bubbles generated at the cathode surface reducing the quality of the deposited film.

4.3 Characterization of Nano-Composite Films with PDDA Polymer Matrix

4.3.1 Thermogravimetric Analysis

Samples P1-6 through P1-10, P2-5 and P2-6 were analyzed by thermogravimetric analysis (TGA). The results of the P1 Series of samples and a PDDA sample are shown in Figure 4.1a. The PDDA sample shows a 98% weight reduction by 950 C. The majority of weight reduction observed for P1 Series samples occurred between 25 and 500°C. A decrease in retained weight was observed with an increase in the deposition polymer solution concentration. Table 4.1 displays the weight reduction at 1200°C. Figure 4.1 shows TGA results for samples P1-8, P2-5 and P2-6, deposited with 0.6 g/L PDDA solution concentration. Weight reduction at 1200°C varied between 56.42 and 58.94 wt% with an average of 57.70 wt% as shown in Figure 4.1b.

Table 4.1 TGA results

Sample	**Polymer Content in Electrolyte (g/L)**	**Weight Reduction, (wt %)**
P1-6	0	22.47
P1-7	0.4	44.93
P1-8	0.6	57.64
P2-5	0.6	58.94
P2-6	0.6	56.52
P1-9	0.8	59.42
P1-10	1.2	71.39

4.3.2 Scanning Electron Microscopy

Figures 4.2, 4.3 and 4.4 show SEM images obtained from sample P1-13. Submersion in liquid nitrogen caused the film to crack and delaminate in some areas as shown in Figures 4.2 and 4.3. Figure 4.4 displays a cross-section of an undamaged region of the film. The film thickness measured, from the cross-section micrograph, was approximately 1.5 μm. Film thickness obtained by the cross-section of P1-12 was also approximately 1.5 μm.

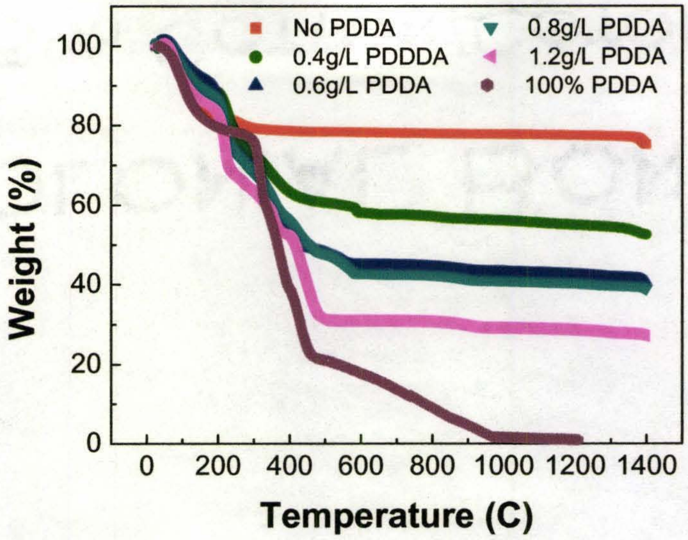

(a)

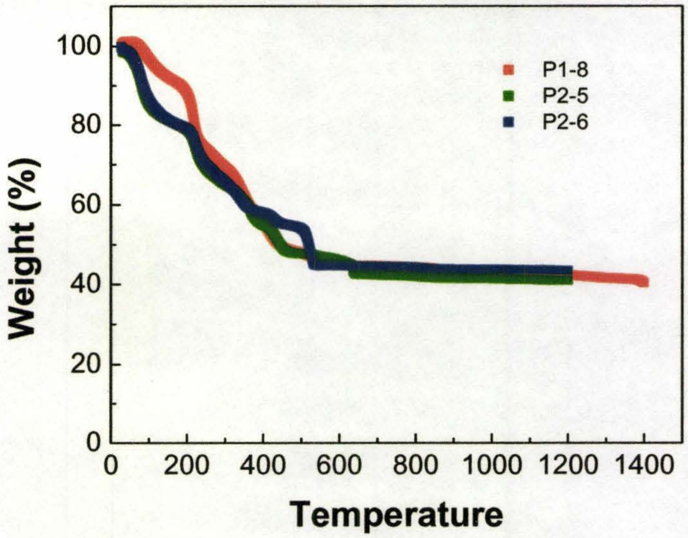

(b)

Figure 4.1 TGA results for (a) P1 Series, (b) Samples P1-8, P2-5, P2-6 made with 0.6 g/L PDDA.

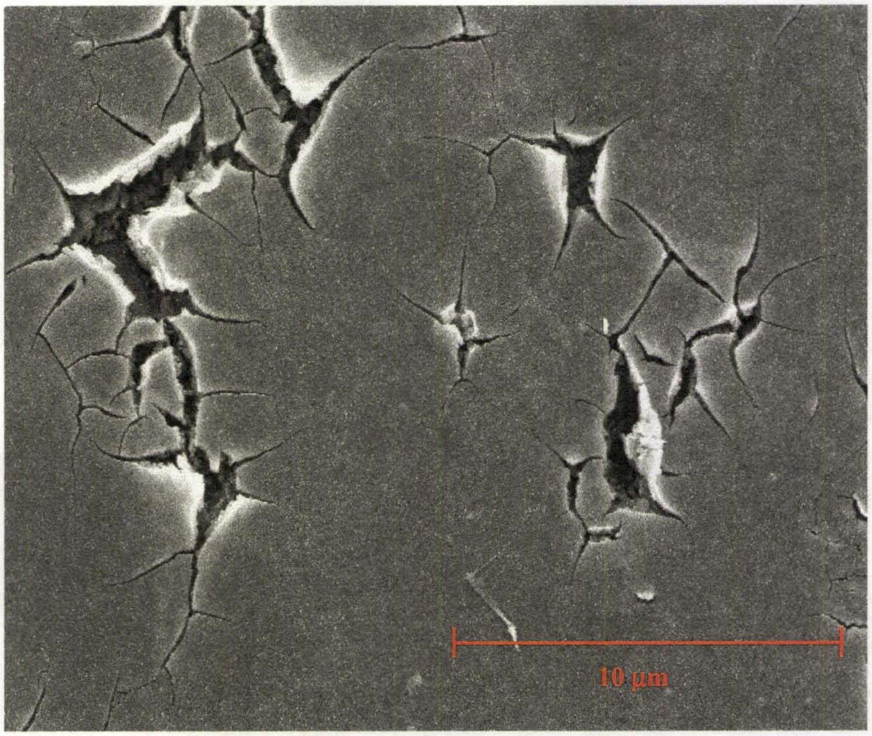

Figure 4.2 SEM image of Sample P1-13 showing surface-on view of the film.

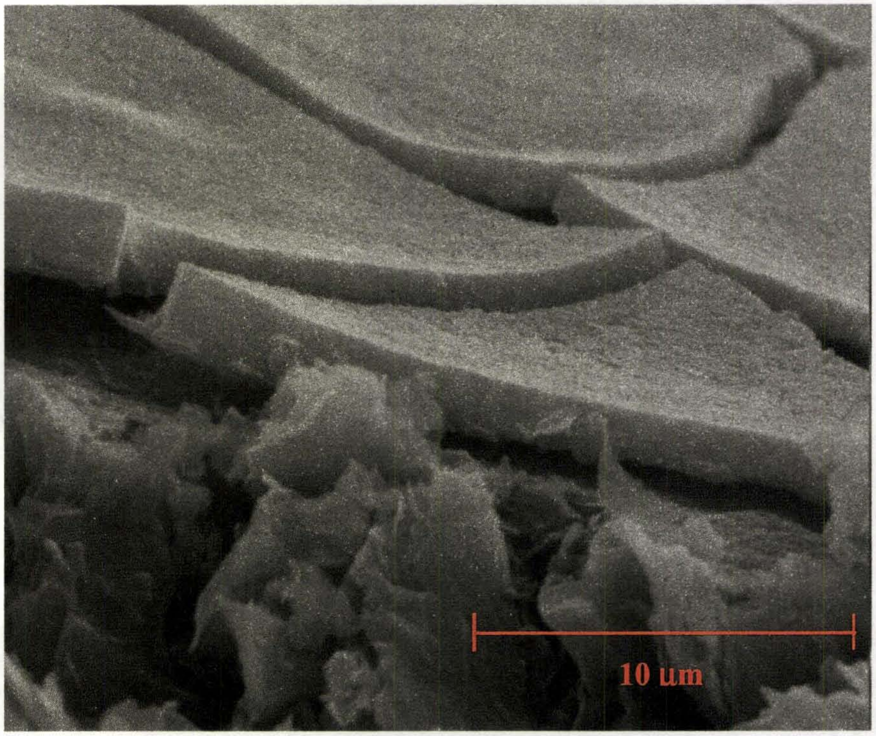

Figure 4.3 SEM image of Sample P1-13 showing cross-section of delaminated film.

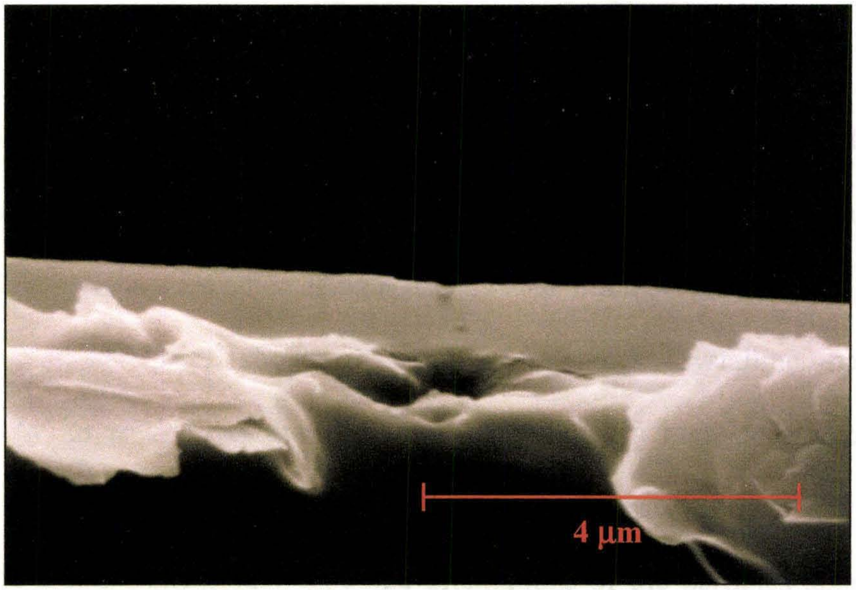

Figure 4.4 SEM image of Sample P1-13 showing cross-section of the film and substrate.

4.3.3 Atomic Force Microscopy

Figure 4.5 shows an AFM topography image obtained from sample P1-11. The deposited film was reasonably smooth with a surface roughness of RMS = 5.695 nm.

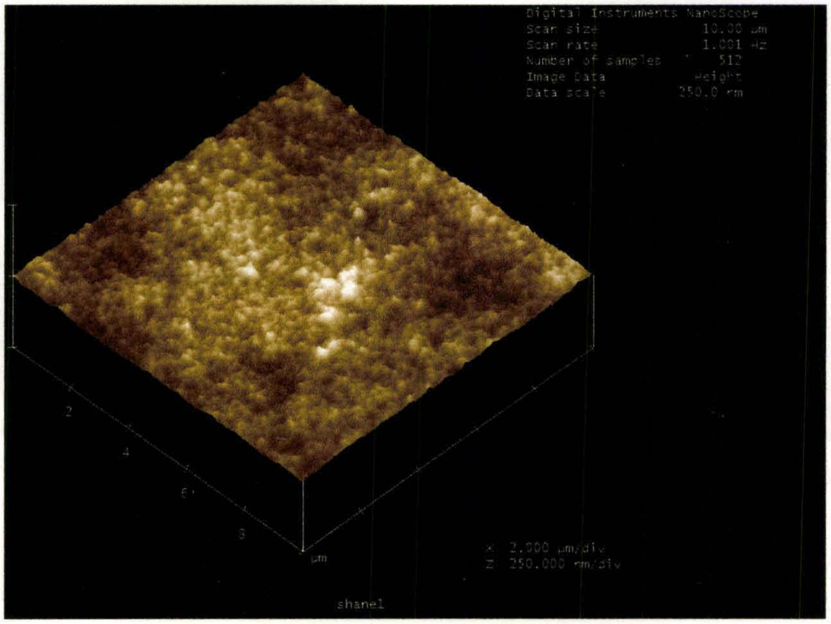

Figure 4.5 AFM image showing topography of Sample P1-11

4.3.4 Transmission Electron Microscopy

TEM images were provided by I. Zhitomirsky and M. Niewzcas. TEM samples were prepared of a deposit from 0.5 g/L PPDA solution concentration on a carbon felt cathode. TEM images were taken using a JEOL 2010F microscope.

The HREM image, shown in Figure 4.6, shows crystalline, nano-particles surrounded by an amorphous matrix. The image shows a high density of randomly distributed particles. Particles are spherical with an observed particle diameter in the order of 4 to 5 nm. The crystallographic orientations of the particles appear random. Interparticle spacing is quite small and in some cases was observed less than 1 nm.

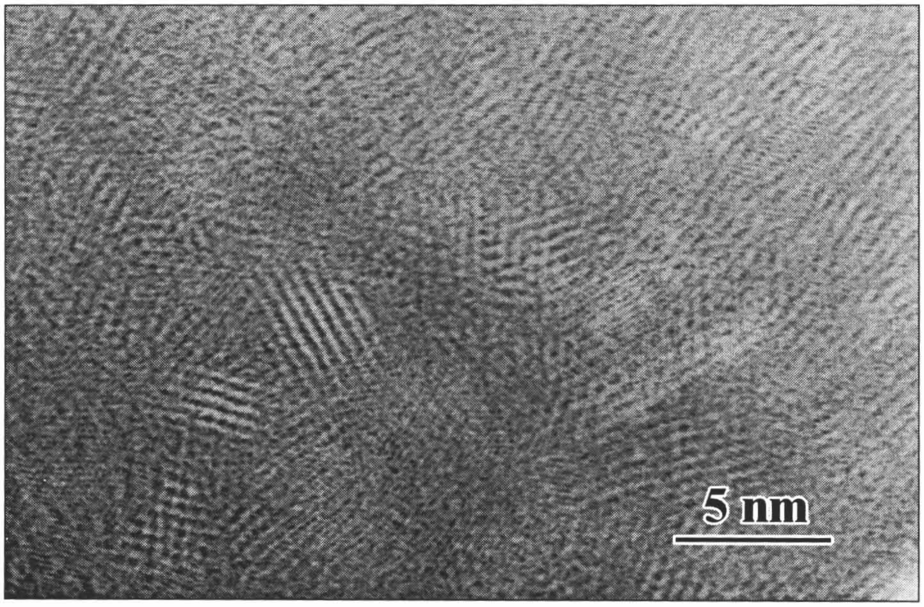

Figure 4.6 HREM image of film prepared with 0.5 g/L PDDA solution. Image provided by I. Zhitomirsky and M. Niewczas.

4.3.5 X-Ray Diffraction

X-ray diffraction results are shown in Figure 4.7. A broad peak is seen in all three samples centered at approximately $2\theta = 35°$ which matches the major peak of magnetite and maghemite. Figure 4.7c shows two sharp peaks at $2\theta = 39$ and $2\theta = 46°$ indicating the presence of platinum.

4.3.6 Magnetic Measurements

Figure 4.8 displays magnetization of the P1 Series at both low and high applied fields. Sample P1-1, containing no PDDA, showed hysteresis behaviour below 50 K and 20 K for low and high fields respectively. Above these temperatures, P1-1 showed no remnant magnetization consistent with superparamagnetic magnetization. At low fields, magnetic behaviour showed relatively constant susceptibility at and above 50 K analogous to paramagnetic behaviour (but much higher susceptibility). At high fields, P1-1 showed paramagnetic behaviour at 298 K. Magnetization decreased with an increase in temperature.

Samples P1-2 through P1-5 showed hysteresis behaviour below a blocking temperature. Above the blocking temperature the samples displayed non-hysteresis behaviour with the absence of a coercive field and remanent magnetization. At low temperatures above the blocking temperature, the curve exhibited superparamagnetic behaviour but approached constant susceptibility, paramagnetic behaviour as

Figure 4.7 XRD results. (a) P1-14, no PDDA, (b) P1-15, 0.4 g/L PDDA and (c) P2-7, 0.4 g/L PDDA.

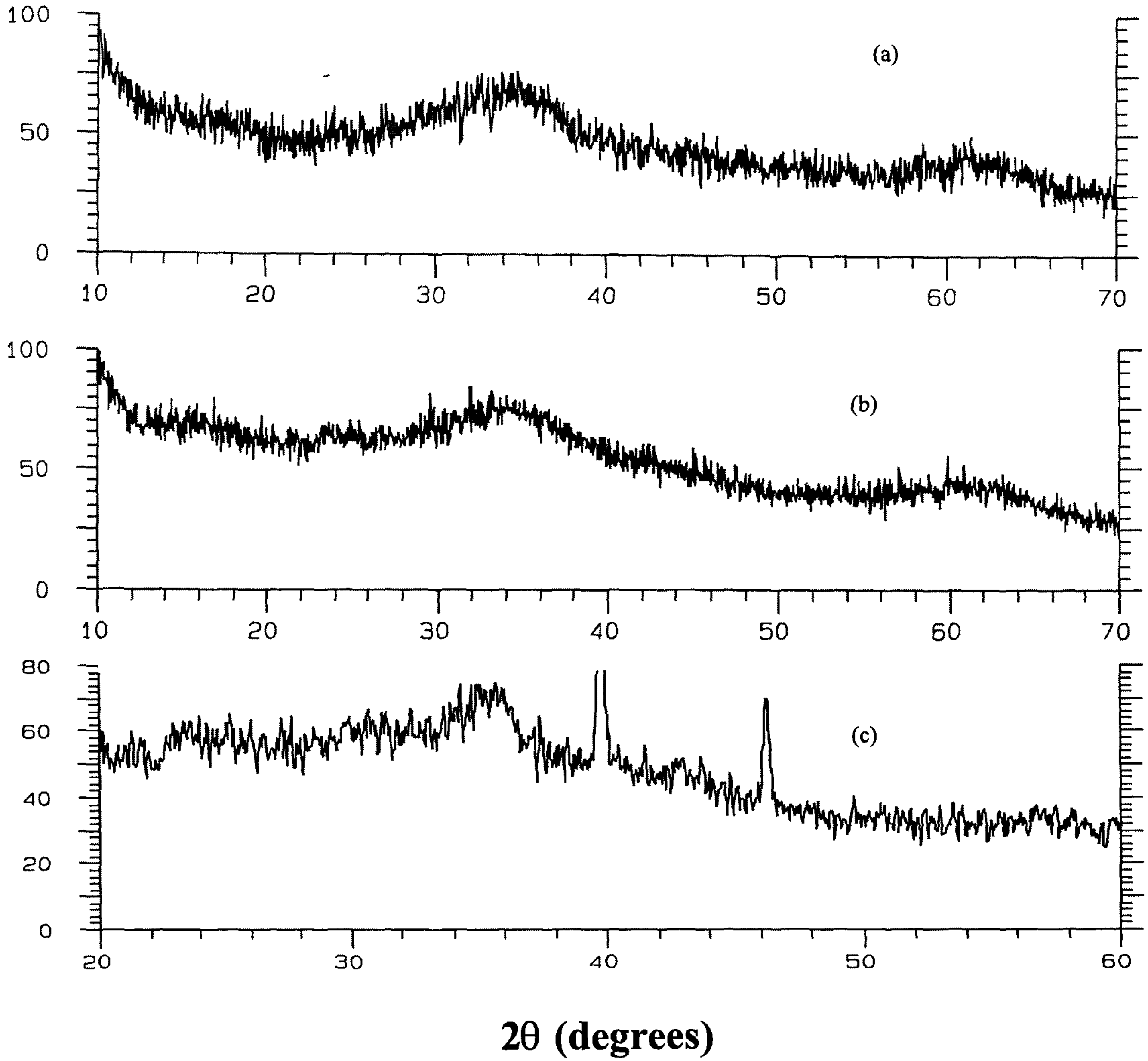

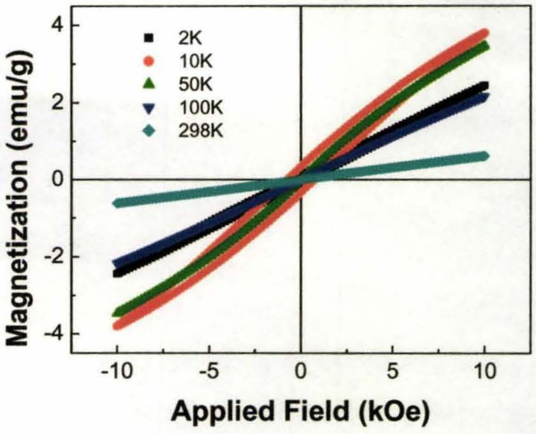
Magnetization (emu/g)
Applied Field (kOe)
2K
10K
50K
100K
298K
4
2
0
-2
-4
-10
-5
0
5
10

(a)

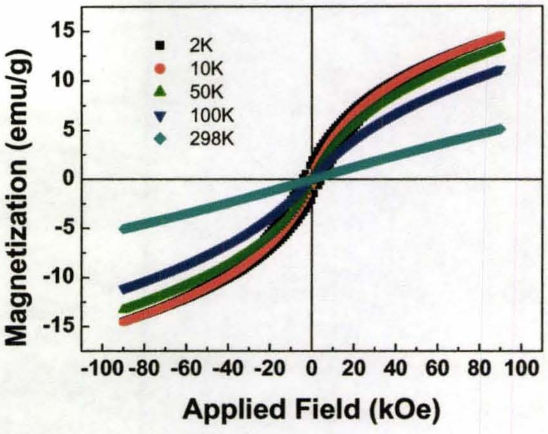
Magnetization (emu/g)
Applied Field (kOe)
2K
10K
50K
100K
298K
15
10
5
0
-5
-10
-15
-100
-80
-60
-40
-20
0
20
40
60
80
100

(b)

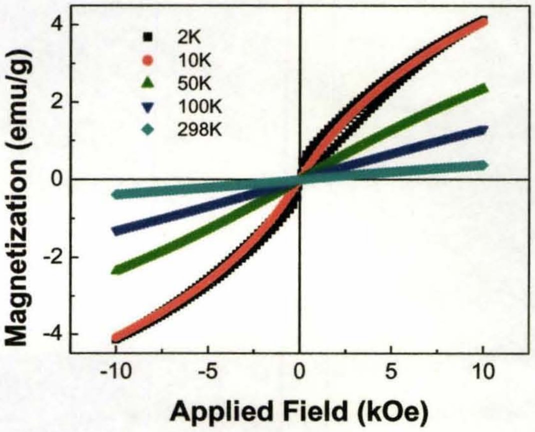
Magnetization (emu/g)
Applied Field (kOe)
2K
10K
50K
100K
298K
4
2
0
-2
-4
-10
-5
0
5
10

(c)

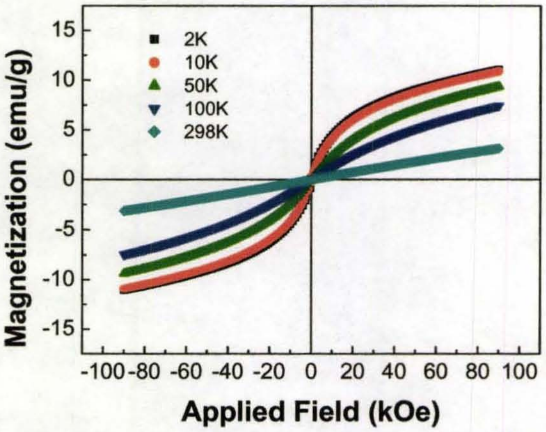
Magnetization (emu/g)
Applied Field (kOe)
2K
10K
50K
100K
298K
15
10
5
0
-5
-10
-15
-100
-80
-60
-40
-20
0
20
40
60
80
100

(d)

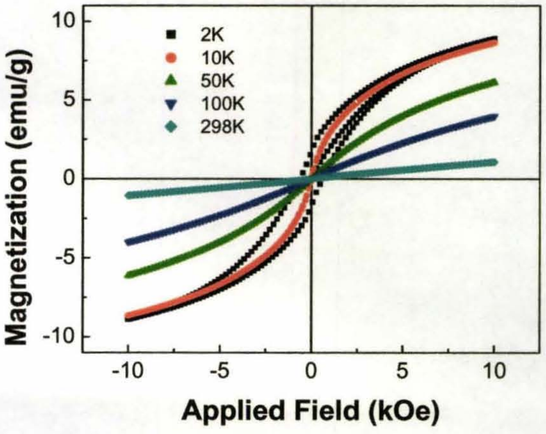
Magnetization (emu/g)
Applied Field (kOe)
2K
10K
50K
100K
298K
10
5
0
-5
-10
-10
-5
0
5
10

(e)

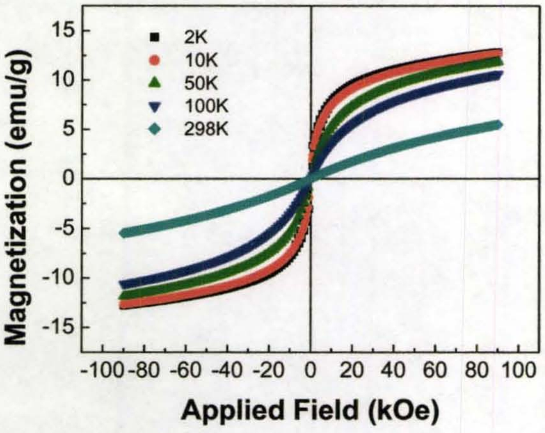
Magnetization (emu/g)
Applied Field (kOe)
2K
10K
50K
100K
298K
15
10
5
0
-5
-10
-15
-100
-80
-60
-40
-20
0
20
40
60
80
100

(f)

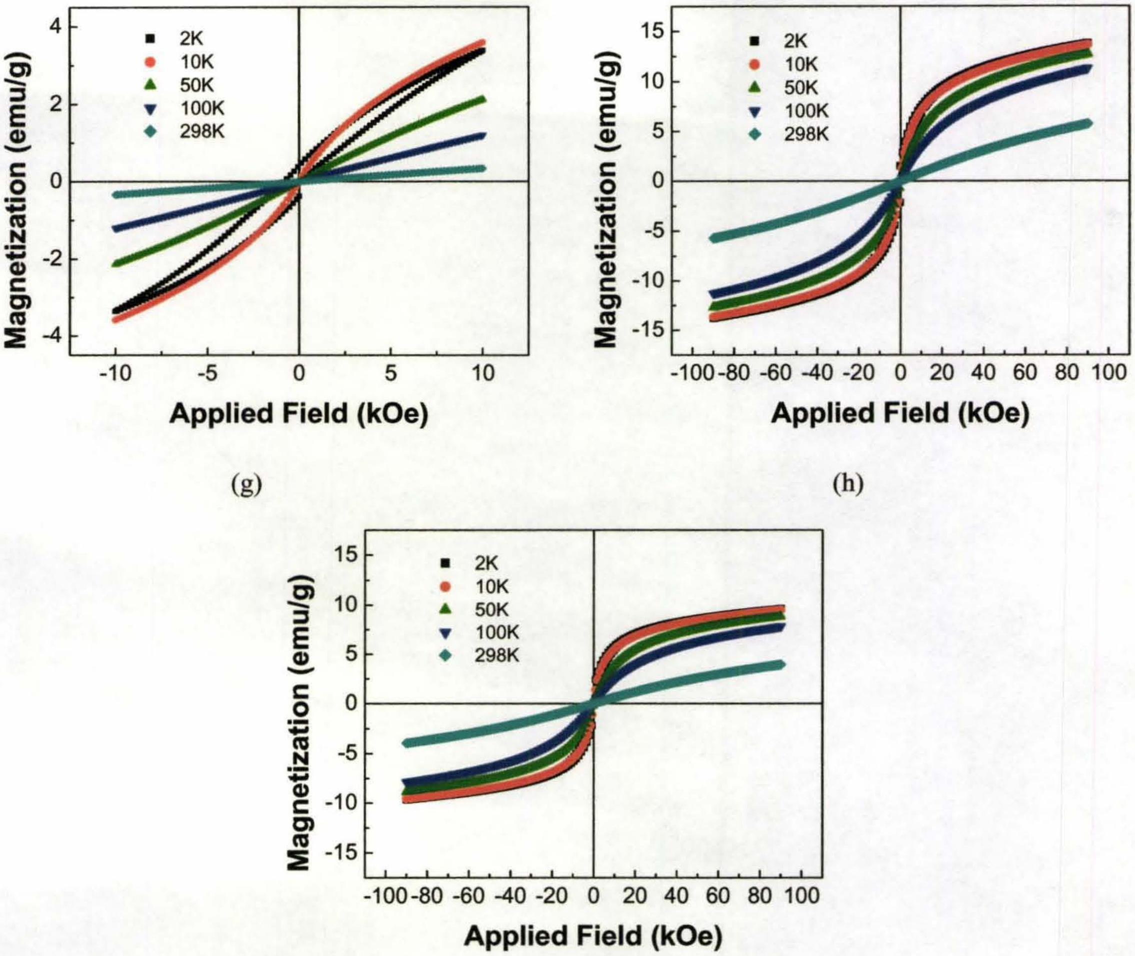

(g)

(h)

(i)

Figure 4.8 Magnetization versus applied field characteristics for P1 Series. (a) P1-1, no PDDA, low field, (b) P1-1, high field, (c) P1-2, 0.4 g/L PDDA, low field, (d) P1-2, high field, (e) P1-3, 0.6 g/L PDDA, low field, (f) P1-3, high field, (g) P1-4, 0.8 g/L PDDA, low field, (h) P1-4, high field, (i) P1-5, 1.2 g/L PDDA, high field.

temperature increased. Magnetization showed a continuous increase throughout the tested field range, even at high fields. Magnetization decreased with an increase in temperature.

At low fields, Sample P1-3 showed nearly twice the magnetization as Samples P1-2 and P1-4. At high fields, Samples P1-2, P1-3 and P1-4 showed magnetization within same range. P1-1, containing no polymer, showed the highest magnetization of the P1 Series at low temperatures.

Figure 4.9 displays the high field magnetization results from the P2 Series. Sample P2-1 showed a similar behaviour as P1-1. P1-1 displayed hysteresis magnetization at temperatures below 15 K. No remanent magnetization was observed at 15 K or higher. The magnetization showed Langevin behaviour until 298 K where the magnetization behaved as paramagnetic.

Composite materials in the P2 Series displayed very different magnetization from the P1 Series. Samples P2-2, P2-3 and P2-4 showed very high initial susceptibilities followed by a plateau at low fields. Above the blocking temperatures, samples exhibited non-hysteresis magnetic behaviour consistent with superparamagnetic magnetization. Samples showed superparamagnetic behaviour between the blocking temperature and 298 K. Composite films in the P2 Series showed higher magnetization than the P1 Series.

ZFC and FC results for samples from the P1 Series are shown in Figure 4.10. ZFC curves showed an increase in magnetization at low temperatures, a maximum in magnetization, followed by a decrease in magnetization as per the Curie-Weiss Law. Samples P1-3 and P1-4 FC showed a continuous decrease in magnetization and below the breaking temperature decreased following Curie-Weiss behaviour.

Samples P1-1 and P1-2 showed a decrease in M_{FC} at low temperatures to a local minimum in magnetization. Both samples showed breaking temperatures below the peak

M_{ZFC} temperature. At temperatures above the M_{ZFC} peak temperature the magnetization decreased by Curie-Weiss behaviour.

All samples showed relaxation as the ZFC and FC curve superimposed below a breaking temperature. Only a small difference between maximum M_{ZFC} temperatures and breaking temperatures were observed. Table 4.2 lists the maximum M_{ZFC}, the temperature of the maximum M_{ZFC} and M_{FC} at 2 K.

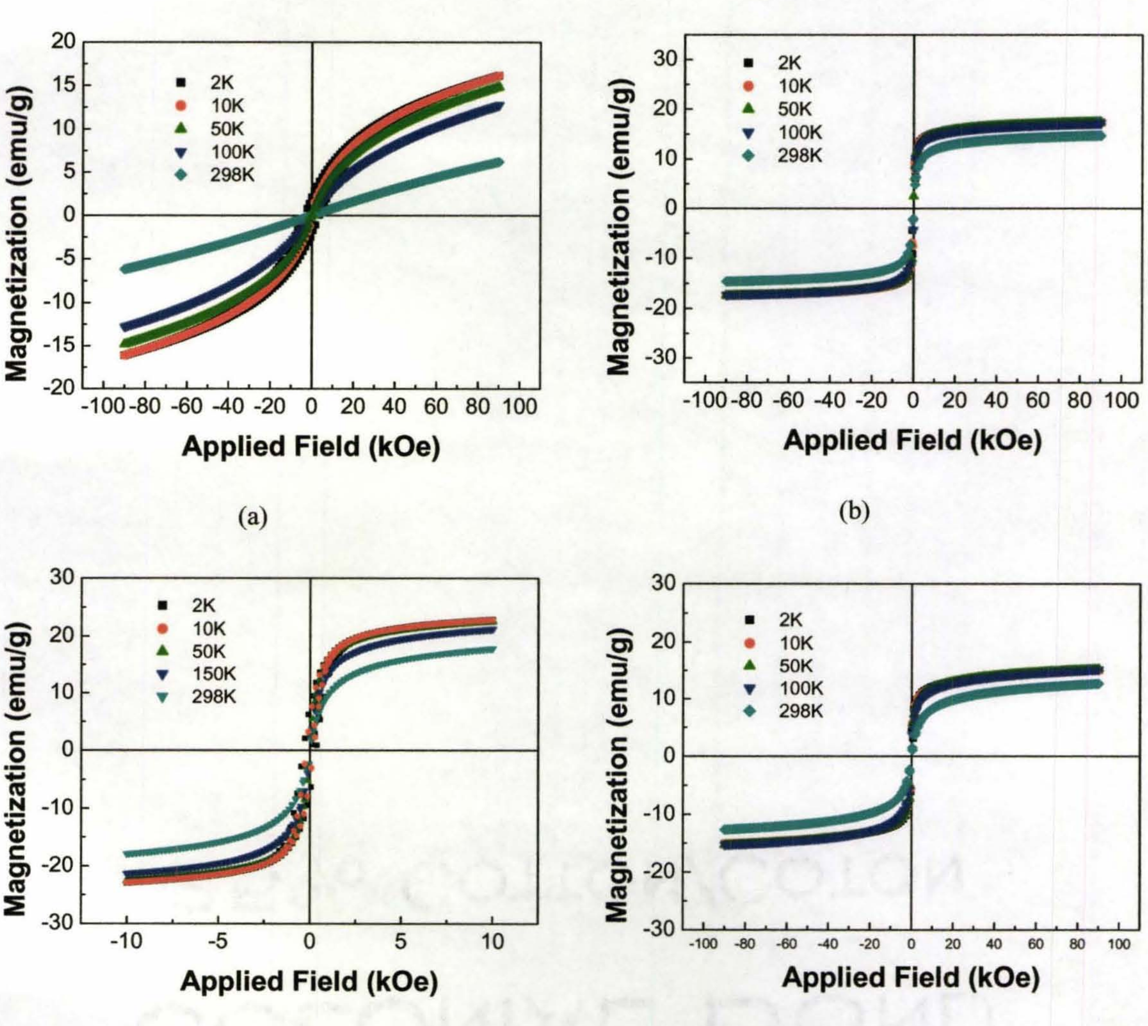

(a) (b)

(c) (d)

Figure 4.9 Magnetization versus applied field characteristics for P2 Series. (a) P2-1, no PDDA, high field, (b) P2-2, 0.4 g/L PDDA, high fieldC (c) P2-3, 0.6 g/L PDDA, high field, (d) P2-4, 0.8 g/L PDDA, high field.

Figure 3.11 shows ZFC and FC results for the P2 Series. ZFC behaviour shows an increase at low temperatures to a maximum magnetization in all samples. ZFC and FC plots are superimposed above a breaking temperature. Sample P1-1 showed a M_{ZFC} and M_{FC} decrease as per the Curie-Weiss Law at temperatures above the peak ZFC magnetization. Samples P2-2, P2-3 and P2-4 do not exhibit Curie-Weiss behaviour. Sample P2-3 showed a linear decrease in magnetization with an increase in temperature above the peak magnetization. Samples P2-2 and P2-4 show only a slight deviation from a linear decrease in magnetization with an increase in temperature.

Sample P2-1 displayed a local M_{FC} minimum below the breaking temperature. P2-1 exhibited a breaking temperature below the maximum M_{ZFC} temperature. Sample P2-1 shows similar magnetic characteristics to Sample P1-1.

Composite P2 samples showed a continuous M_{FC} decrease at low temperatures. Samples P2-3 and P2-4 showed only a small decrease in M_{FC} from 2 K to the breaking temperature. Differences in M_{FC} at 2 K and the peak M_{ZFC} were typically less than 1 emu/g.

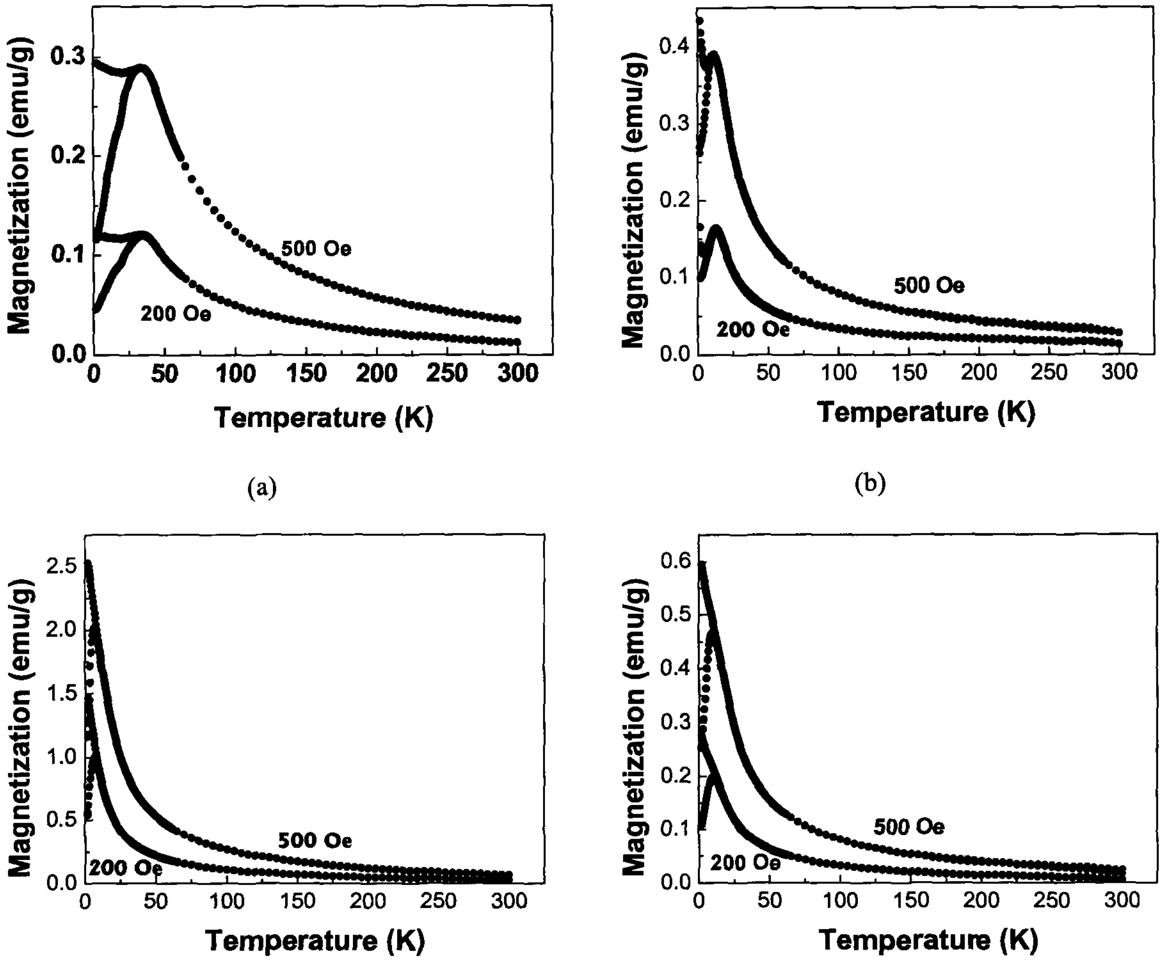

(a) (b)

(c) (d)

Figure 4.10 ZFC and FC characteristics for P1 Series. (a) P1-1, no PDDA, (b) P1-2, 0.4 g/L PDDA, (c) P1-3, 0.6 g/L PDDA, (d) P1-4, 0.8 g/L PDDA.

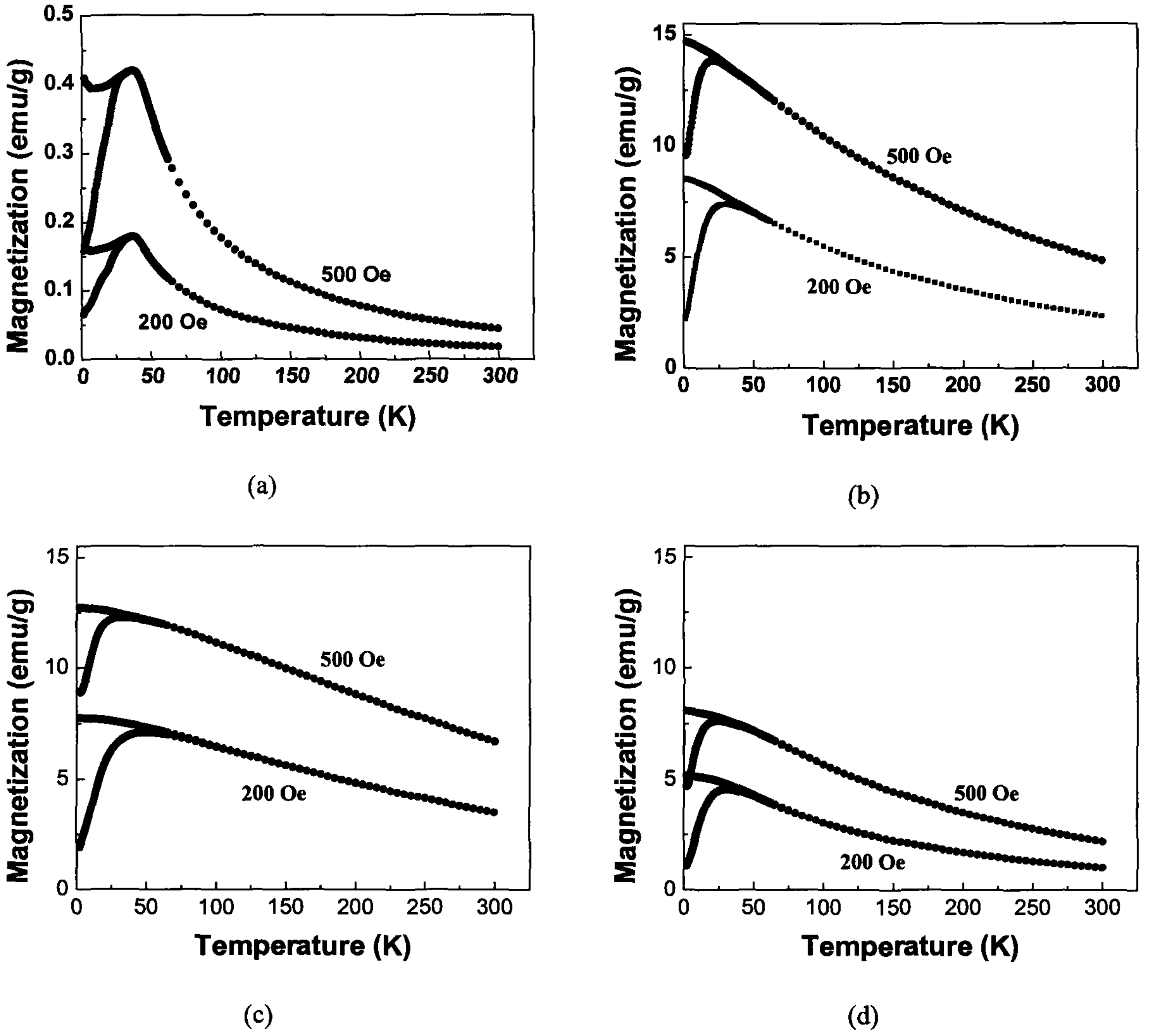

(a)

(b)

(c)

(d)

Figure 4.11 ZFC and FC characteristics for P2 Series. (a) P2-1, no PDDA, (b) P2-2, 0.4 g/L PDDA, (c) P2-3, 0.6 g/L PDDA, (d) P2-4, 0.8 g/L PDDA.

Table 4.2 ZFC and FC summary for P1 and P2 Series

Sample	**200 Oe Field**			**500 Oe Field**		
	Max M_{ZFC} (emu/g)	**T at max M_{ZFC} (K)**	**M_{FC} at 2K (emu/g)**	**Max M_{ZFC} (emu/g)**	**T at max M_{ZFC} (K)**	**M_{FC} at 2K (emu/g)**
P1-1	0.12	34.52	0.12	0.29	34.51	0.29
P1-2	0.16	13.52	0.10	0.39	11.50	0.43
P1-3	0.99	6.93	1.47	2.01	6.43	2.53
P1-4	0.20	9.97	0.276	0.47	9.97	0.59
P2-1	0.18	36.54	0.17	0.42	36.53	0.41
P2-2	7.43	29.00	8.54	13.86	21.48	14.69
P2-3	7.08	51.07	7.76	12.26	31.51	12.74
P2-4	4.55	31.01	5.17	7.62	24.49	8.08

Figure 4.12 displays the real (χ') and imaginary (χ'') components of AC susceptibility measurements of the P1 Series. χ' versus temperature curves showed an initial increase to a peak value followed by a decrease at an inverse relation with temperature. χ' measurements at low frequencies provided cluttered values. Samples P1-1, P1-2 and P1-4 showed χ' values within the same order whereas Samples P1-3 and P1-5 showed real susceptibility an order of magnitude higher. Sample P1-3 displayed the highest real component of susceptibility from the P1 Series. Samples P1-1, P1-2 and P1-4 showed only minor decrease in χ' with an increase in frequency. Samples P1-3 and P1-5 showed a larger but still small decrease in χ' with increasing frequency.

All samples showed a small increase in the peak χ' temperature, T_{max} with an increase in frequency. Sample P1-1 showed the highest T_{max} values of 39 and 40 K at 10 and 10 000 Hz. Composite samples from the P1 Series displayed T_{max} values between 9 and 17 K at tested frequencies. P1-3 showed the lowest T_{max} values from the P1 Series.

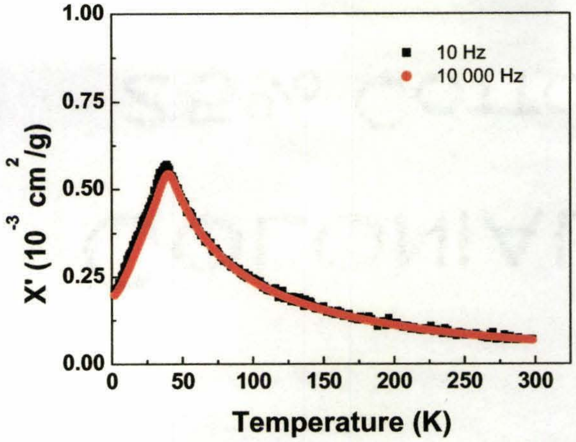
1.00
0.75
0.50
0.25
0.00
X' (10^-3 cm^2/g)
0
50
100
150
200
250
300
Temperature (K)
10 Hz
10 000 Hz

(a)

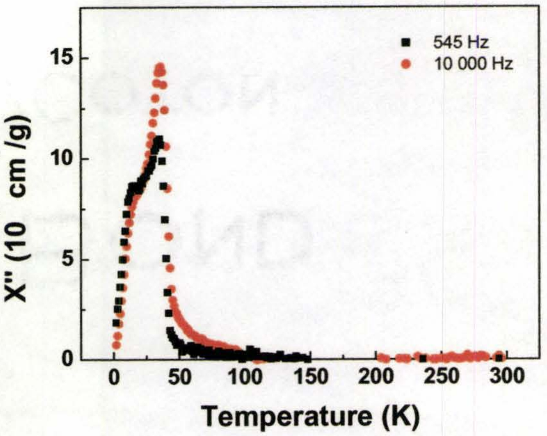
15
10
5
0
X'' (10^-6 cm^2/g)
0
50
100
150
200
250
300
Temperature (K)
545 Hz
10 000 Hz

(b)

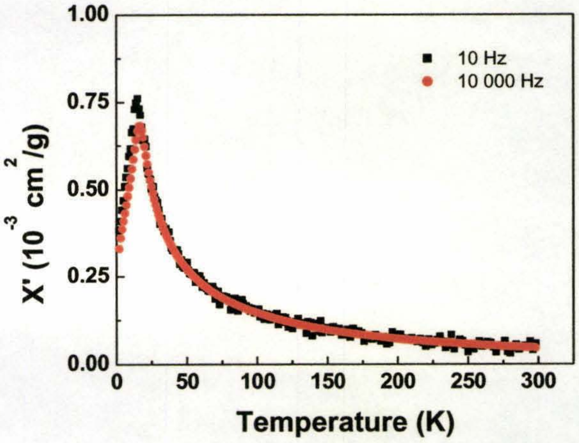
1.00
0.75
0.50
0.25
0.00
X' (10^-3 cm^2/g)
0
50
100
150
200
250
300
Temperature (K)
10 Hz
10 000 Hz

(c)

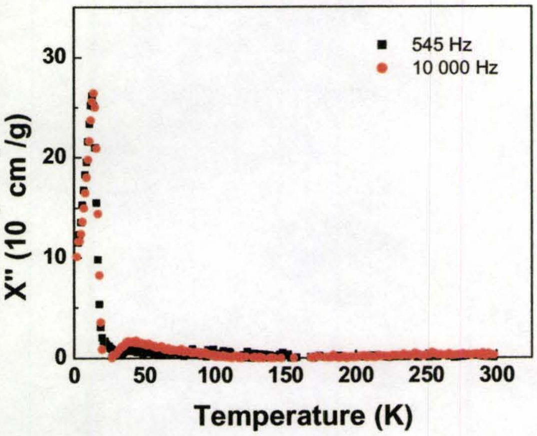
30
20
10
0
X'' (10^-6 cm^2/g)
0
50
100
150
200
250
300
Temperature (K)
545 Hz
10 000 Hz

(d)

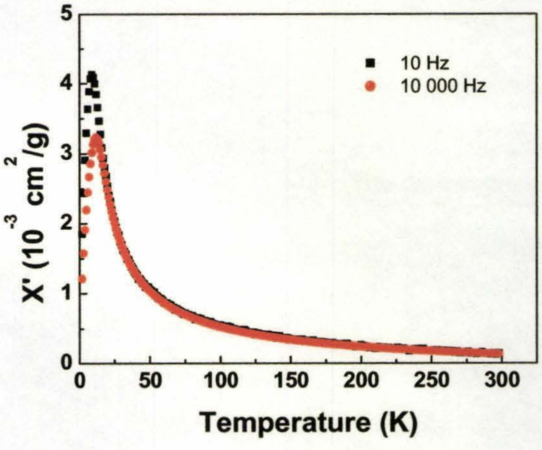
5
4
3
2
1
0
X' (10^-3 cm^2/g)
0
50
100
150
200
250
300
Temperature (K)
10 Hz
10 000 Hz

(e)

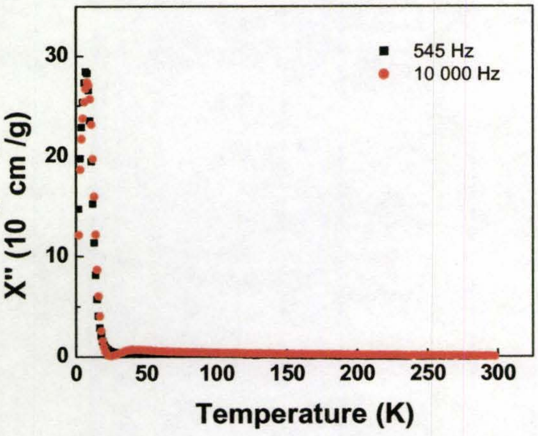
30
20
10
0
X'' (10^-5 cm^2/g)
0
50
100
150
200
250
300
Temperature (K)
545 Hz
10 000 Hz

(f)

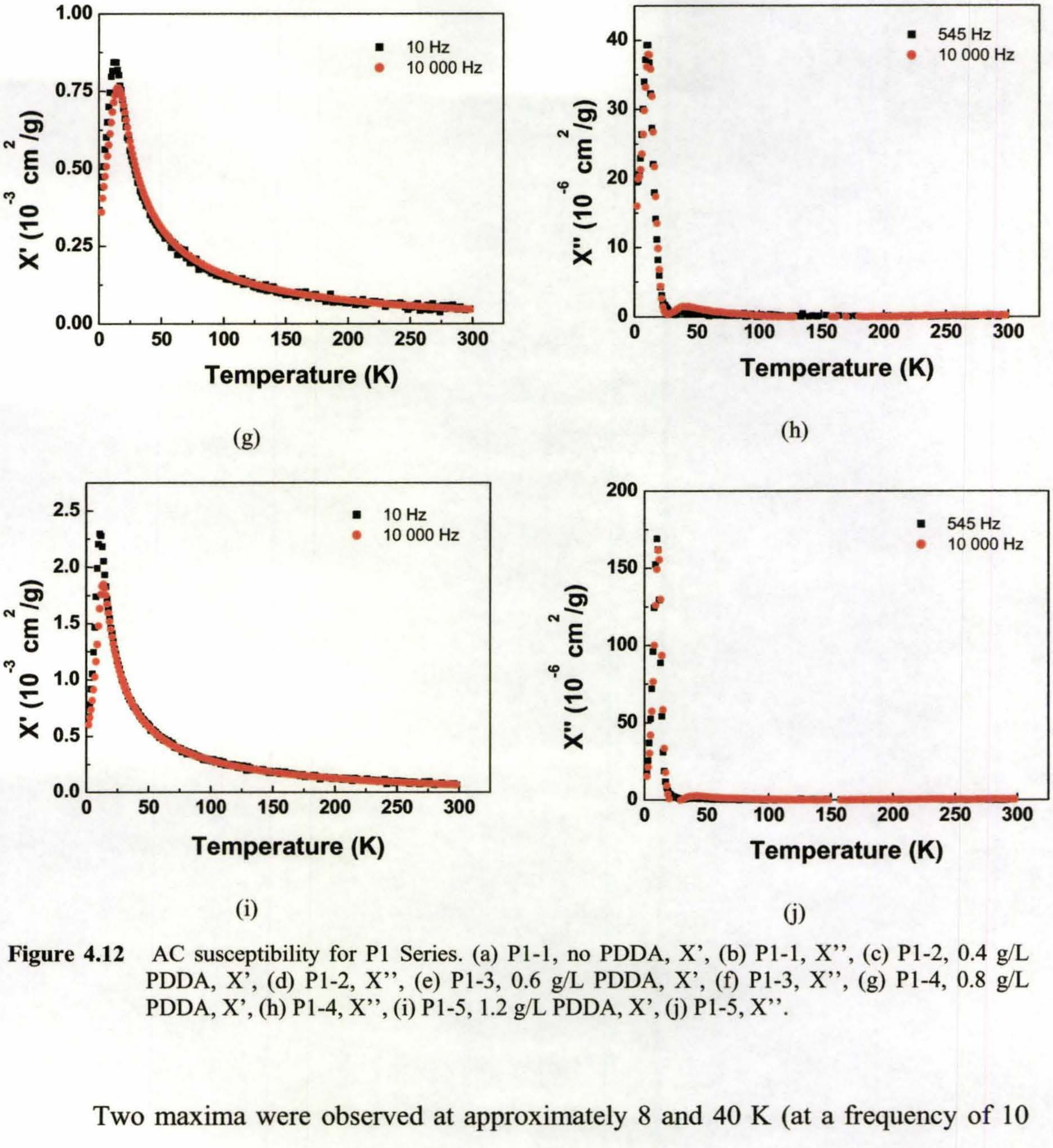

(g) (h)

(i) (j)

Figure 4.12 AC susceptibility for P1 Series. (a) P1-1, no PDDA, X', (b) P1-1, X'', (c) P1-2, 0.4 g/L PDDA, X', (d) P1-2, X'', (e) P1-3, 0.6 g/L PDDA, X', (f) P1-3, X'', (g) P1-4, 0.8 g/L PDDA, X', (h) P1-4, X'', (i) P1-5, 1.2 g/L PDDA, X', (j) P1-5, X''.

Two maxima were observed at approximately 8 and 40 K (at a frequency of 10 000 Hz) in the χ'' versus temperature plot . P1-1 showed the 40 K as most significant and the 8 K peak at approximately half the χ'' value. Composite films showed a major χ'' peak at 8 K with only a minor peak at 40 K. Peak values shifted up only a degree with an increase of frequency in the range of 545 to 10 000 Hz. At temperatures above

50 K, χ'' approached zero. Samples P1-1, P1-2, P1-3 and P1-4 showed χ'' values with the same range. Sample P1-5 showed imaginary susceptibility values an order of magnitude higher.

Real and imaginary components of the AC susceptibility from the P2 Series are displayed in Figure 4.13. Sample P2-1 shows similar characteristics as Sample P1-1 but with a higher χ'.

Composite samples from the P2 Series showed higher χ' values than the P1 Series and Sample P2-1. T_{max} increased between 11 to 15 K with an increase from 10 to 10 000 Hz for P2 composite samples. Sample P2-3 showed the highest T_{max} at 96 and 111 K at 10 and 10 000 Hz respectively. χ' decreased with an increase in frequency. Composite samples showed a decrease in χ' with an increase in frequency.

χ'' values for the composite materials were two orders of magnitude higher than for Sample P2-1. P2-1 showed similar χ'' characteristics as Sample P1-1. Composite samples showed only one χ'' peak and peak temperatures decreased with an increase in frequency. Composite samples showed a decrease in χ'' with an increase in frequency. Measurements at low frequencies were scattered.

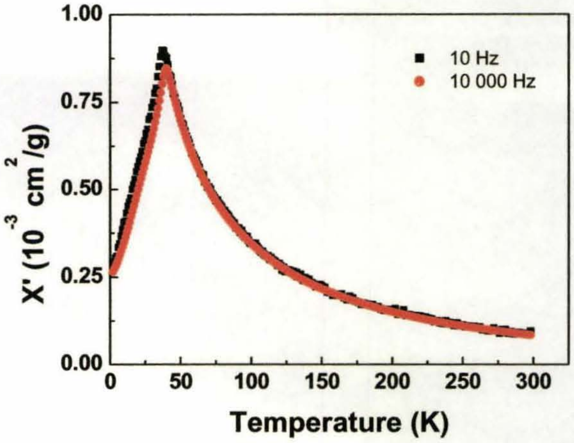
1.00
0.75
0.50
0.25
0.00
X' (10^{-3} cm^2/g)
0
50
100
150
200
250
300
Temperature (K)
10 Hz
10 000 Hz

(a)

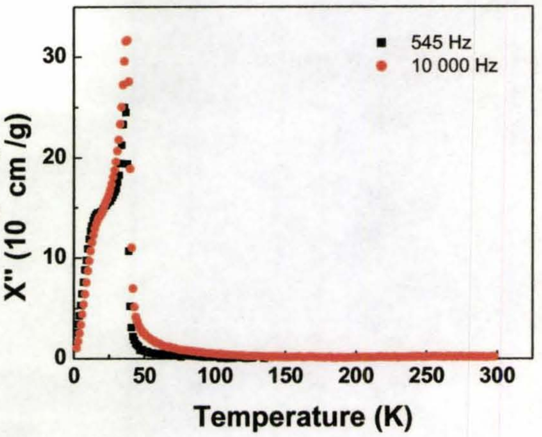
30
20
10
0
X'' (10^{-6} cm^2/g)
0
50
100
150
200
250
300
Temperature (K)
545 Hz
10 000 Hz

(b)

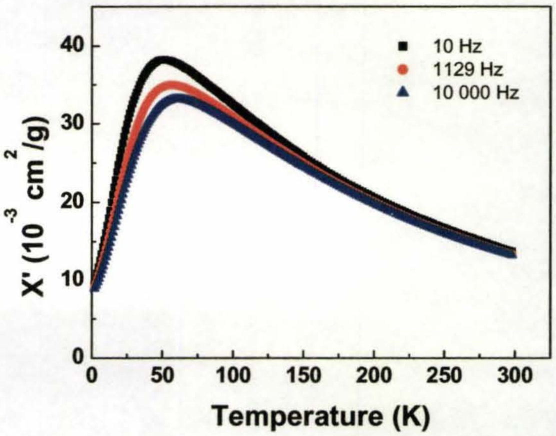
40
30
20
10
0
X' (10^{-3} cm^2/g)
0
50
100
150
200
250
300
Temperature (K)
10 Hz
1129 Hz
10 000 Hz

(c)

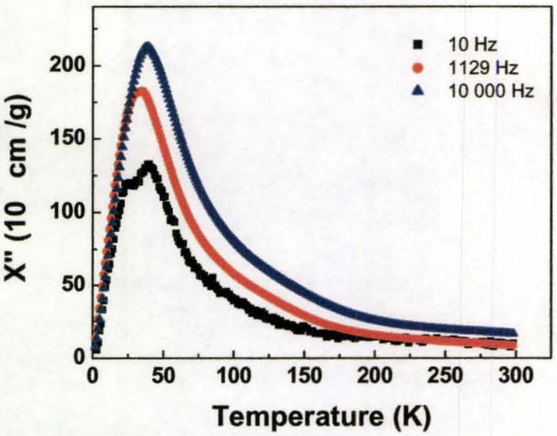
200
150
100
50
0
X'' (10^{-5} cm^2/g)
0
50
100
150
200
250
300
Temperature (K)
10 Hz
1129 Hz
10 000 Hz

(d)

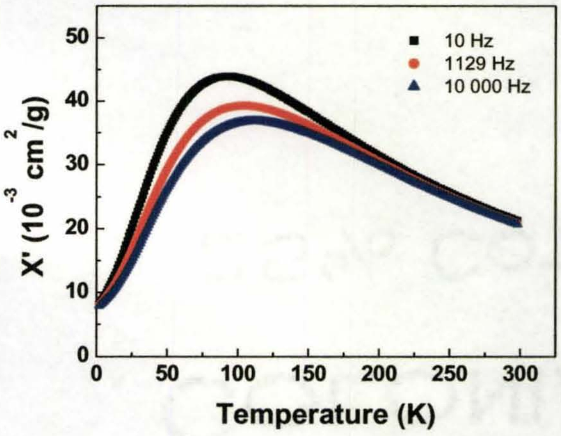
50
40
30
20
10
0
X' (10^{-3} cm^2/g)
0
50
100
150
200
250
300
Temperature (K)
10 Hz
1129 Hz
10 000 Hz

(e)

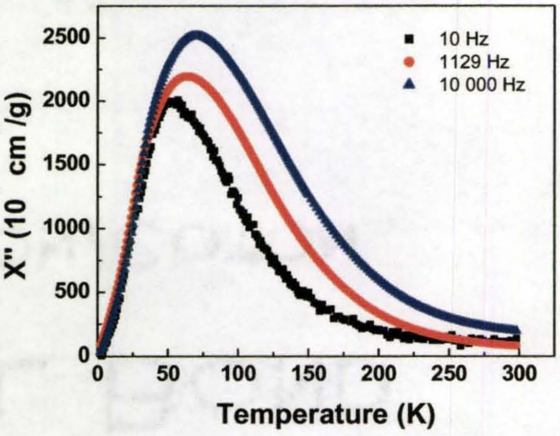
2500
2000
1500
1000
500
0
X'' (10^{-6} cm^2/g)
0
50
100
150
200
250
300
Temperature (K)
10 Hz
1129 Hz
10 000 Hz

(f)

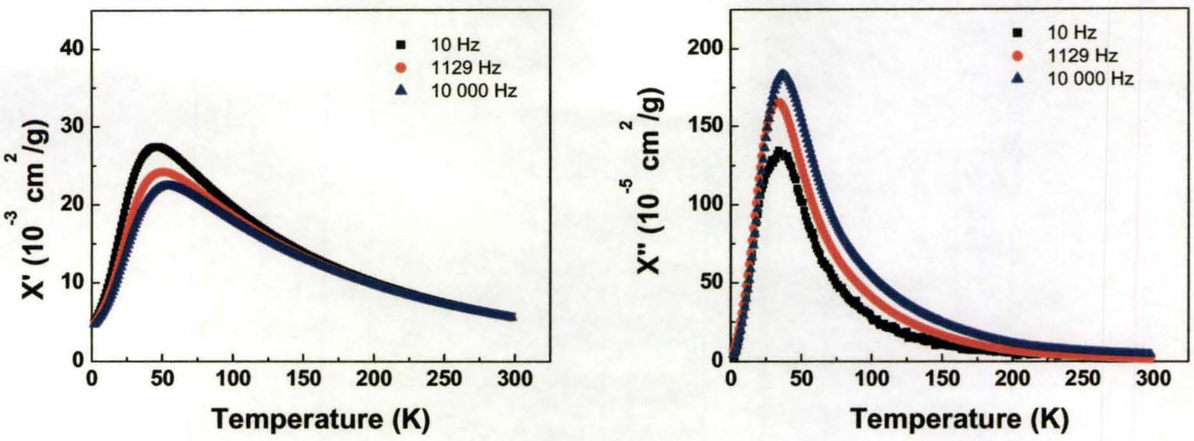

(g) (h)

Figure 4.13 AC susceptibility for P2 Series. (a) P2-1, no PDDA, X', (b) P2-1 X'', (c) P2-2, 0.4 g/L PDDA, X', (d) P2-2, X'', (e) P2-3, 0.6 g/L PDDA, X', (f) P2-3, X'', (g) P2-4, 0.8 g/L PDDA, X', (h) P2-4, X''.

CHAPTER 5

DISCUSSION

5.1 Deposition of Nano-Composite Films

5.1.1 Deposition Theory of Nano-Composite Films

A significant amount of studies and reviews exist for electrolytic and electrophoretic deposition and a reasonable understanding of the two processes exist. (Omer, 1999; Sarkar, 1996; Zhitomirsky, 2000). However, only a few studies using both electrodeposition processes simultaneously exist (Zhitomirsky , 1999, 2000, 2001, 2002; Ulberg, 1992). Zhitomirsky has provided the most relevant theory explaining combined electrolytic and electrophoretic deposition of oxide particles using PDDA (Zhitomirsky, 2002), but for reasons explained below, deposition done within this research does coincide with the model's assumptions. To explain the deposition mechanism of nano-sized Fe_3O_4 particles surrounded by a polymer matrix, an intermediate step must be included within this theory.

Dissolved iron ions, both Fe^{2+} and Fe^{3+}, are attracted to the cathode via traditional electrolytic transport. Due to the reduction of water by the cathodic reaction (Kuhn, 1983; Zhitomirsky, 2002):

$$2H_2O + 2e^- \rightarrow H_2 + 2OH^- \qquad (5.1)$$

the region near the cathode has a high concentration of OH^- molecules and, as a result, has a high pH level (Kuhn, 1983). Under an oxygen free atmosphere and a stoichiometric ferrous/ferric ion concentration, thermodynamic modeling predicts the formation of Fe_3O_4 at pH levels greater than 7.5 by the reaction (Kim, 2001):

$$Fe^{2+} + 2Fe^{3+} + 8OH^- \rightarrow Fe_3O_4 + 4H_2O \tag{5.2}$$

The formation of Fe_3O_4 at room temperature within an elevated pH level has been experimentally proven (Cornell, 1996; Kim, 2001; Kroll, 1996; Shchukin, 2003). Therefore magnetite particles can be expected to form in the elevated pH zone near the cathode. As the formation of magnetite occurs at pH levels above the isoelectric point of 6.8 pH (Cornell, 1996), the zeta-potential for magnetite is always negative due to OH^- adsorption.

Zhitomirsky's theory explains the deposition of the hybrid film by a heterocoagulation of oppositely charged colloidal particles and PDDA at the cathode surface. The theory assumes the oxide particles are extremely close to the cathode and no further transport of the oxide particles is necessary. This assumption is not necessarily valid in this case. The location of Fe_3O_4 formation is dependent upon the elevated pH levels extending from the cathode. Once the pH is 7.5 or greater, the formation of magnetite can be expected to occur. Between diffusion, electrostatic migration of OH^- and convection stirring from hydrogen bubbles produced by the cathodic reaction, this critical 7.5 pH level may be far enough away from the cathode for iron oxide particles to require further transport to the cathode.

Very little work has been done regarding the pH profile near the cathode. A study done by Slizhis (Slizhis, 1970), although showing the pH gradient from the cathode for various coatings made with similar current densities to our experimental procedure, fails to indicate the time scale of the deposition. The pH profile does show a constant, elevated pH region ranging from 200 to 400 μm in thickness. Other work done by Ovchinnikova and Rotinyan (Ovchinnikova, 1963), although their experimental procedure is vague, indicates the same behaviour with elevated pH region being 2 mm thick. Neither of these two pieces of work can be used directly as their systems are quite different but it can be used to stimulate the idea that the high pH zone is not arbitrarily small.

In the case transport is required to bring the iron oxide particle to the cathode, an intermediate step is required. Once the formation of magnetite has occurred, its negative charge will electrostatically repulse it from the negative cathode, preventing deposition. Therefore, to propose a hypothesis which explains the results of successfully obtaining an iron oxide / polymer coating, it would seem that the positively charged polymers must combine with the magnetite particle to provide a positive charge to the overall magnetite/polymer particle. Cationic polyelectrolytes and magnetite, at pH >6.8, are electrostatically attracted causing the polymer to attach onto the surface of the oxide particle. Transport of the magnetite/polymer particle to the cathode would occur by electrophoresis. The electrostatic repulsion of the coated polymer will be reduced by the negatively charged iron oxide, reducing the double layer energy barrier and final deposition will occur by coagulation. The proposed deposition process is summarized in Figure 5.1.

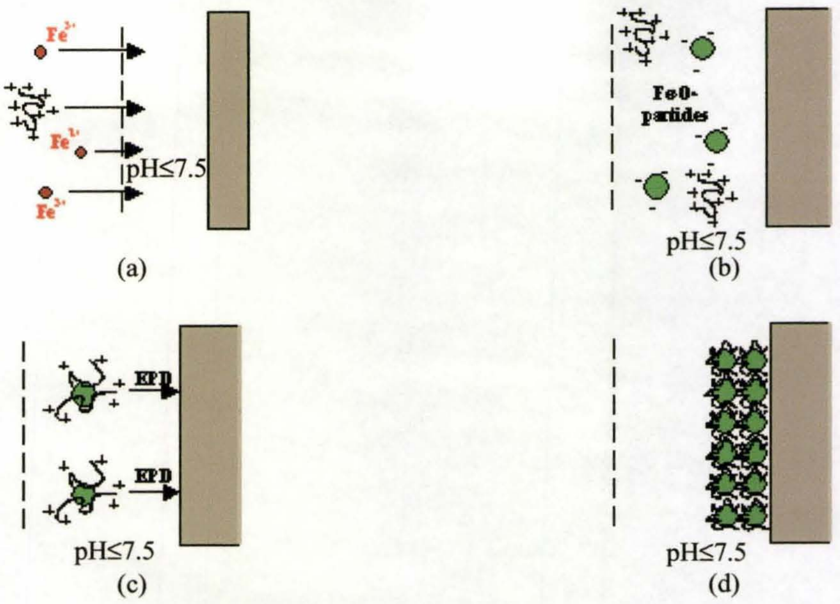

Figure 5.1 Schematics of the deposition of iron oxide/polymer composite films. (a) Iron ions and polymer attracted into high pH zone by the electric field. (b) Formation of Fe_3O4 in $pH \geq 7.5$ zone. (c) Oppositely charged polymer attracted to and bind onto Fe_3O_4, creating a positively charged iron oxide/polymer particle. Iron oxide/polymer particle transported to cathode via EPD. (d) Final deposition and coagulation of iron oxide and polymer onto cathode.

The deposition of a film without the use of polymer cannot be explained by this theory as it depends upon the presence of polymer. Although only a thin film was deposited with only iron ions in solution, the success of deposition indicates a different deposition mechanism. Magnetic properties indicate these films are not entirely an iron oxide and until the nature of these films are understood, their deposition cannot be fully understood. Future work in identifying the composition and phase of the deposit would be necessary in determining potential deposition mechanisms of these films.

5.1.2 Composition of Film and Associated Magnetic Properties

The use of polymer for the deposition and the film's properties was necessary for several reasons: (1) for successful electrodeposition of iron oxide particles, (2) to act as a binder and provide film/substrate adhesion, (3) to prevent nano-particle coagulation and (4) to encapsulate magnetite particles to prevent oxidation once in an air environment.

The polymer concentration within the deposition solution contributes to the magnetic properties of the film: (1) formation/retention of magnetite phase, (2) prevention of particle coagulation, (3) iron oxide to polymer weight ratio, (4) particle size and (5) spacing between particles.

Magnetite is unstable at room temperature in an air environment and will oxidize into hematite over time. A sufficient amount of polymer was expected to act as a barrier for oxygen, maintaining the magnetically favourable magnetite. Sufficient amounts of polymer were required to prevent particles from contacting and agglomerating. Agglomeration can be detrimental to the magnetic properties by increasing the volume above the critical superparamagnetic volume, or, in the case of only two particles coagulating, creating a shape anisotropy which would increase the magnetic reversal energy barrier.

Polymers were considered magnetically insignificant in comparison to iron oxide and polymer magnetic contribution to the magnetic properties of the deposit was assumed negligible. An increase in polymer weight content within the deposit reduced the iron oxide weight content, reducing magnetic properties of the film (when magnetization was measured per unit weight). Polymer composition of the film effected the particle concentration and particle-particle distancing influencing interparticle magnetic interaction.

Polymer concentration was expected to influence the deposited particle size. The particle size must be below a critical volume in order to behave superparmagnetically. Also, at the nano-particle scale, the magnetic dead zone at the surface of the particle includes a significant portion of the particle volume. Reduction is size will increase fraction of iron oxide near the surface of the particle and reduce the magnetically active iron oxide.

As the amount of polymer within the film has contradictory effects upon the magnetic properties of the film, there must be an optimum polymer content within the film at which maximum magnetic properties are obtained. A clear understanding of the deposition mechanisms and conditions leading to deposited film's magnetic properties can be used to engineer films with refined magnetic properties to meet the needs of specific applications.

5.2 Nano-Composite Film using PEI Polymer Matrix

Deposits produced using PEI as matrix polymer showed low adhesion at a current density of 5 mA/cm^2 and low magnetization. Therefore, PEI was considered inferior when compared to PDDA as PDDA had good adhesion at 5 mA/cm^2 made with a 0.4 g/L polymer concentration and showed magnetic properties at all tested polymer contents.

5.3 Nano-Composite Film using PAM-PDDA Polymer Matrix

Interest in PAM-PDDA as the polymer matrix was due to its lower charge than PDDA. The acrylamide group between the diallyldimethylammonium chloride groups reduces the charge per length of the polymer when compared to PDDA. However, PAM-PDDA displayed inadequate adhesion at all of the tested methanol/water mixtures. Due to its poor adhesion, PAM-PDDA was considered inferior to PDDA for the development of nano-composites via this electrodeposition method and work was discontinued with this polymer.

5.4 Nano-Composite Film using PDDA Polymer Matrix

5.4.1 Iron Oxide content of the Films

Thermogravimetric analysis was used to approximate the iron oxide content within the deposited films. TGA showed a 98% weight reduction in a PDDA sample when heated to 950 C. Therefore, most of the weight reduction observed in heating the composite films to 1200 C was assumed as polymer burnout and the retained weight as iron oxide. At 1200 C in an air environment, iron oxide exists in the α-Fe_2O_3 state (Kroll, 1996; Cornell, 1996). Retained weight values are plotted in Figure 5.2a. The decrease in the film's iron oxide content supported the PDDA concentration of the bath solution can be used to manipulate the iron oxide to polymer ratio within the deposited film.

The observed weight loss in P1-6 (no PDDA) was from a different mechanism than the composite films. As films produced without polymer are believed to be mostly iron hydroxide, the observed weight loss seen in Sample P1-6 can partially be attributed to the dehydration of these iron hydroxides into iron oxide.

TGA of Samples P1-8, P2-5 and P2-6, all made with a 0.6 g/L PDDA solution concentration, showed all three samples to have had similar retained weight values at 1200°C. Polymer composition appeared insensitive to the experimental differences between P1 and P2 Series.

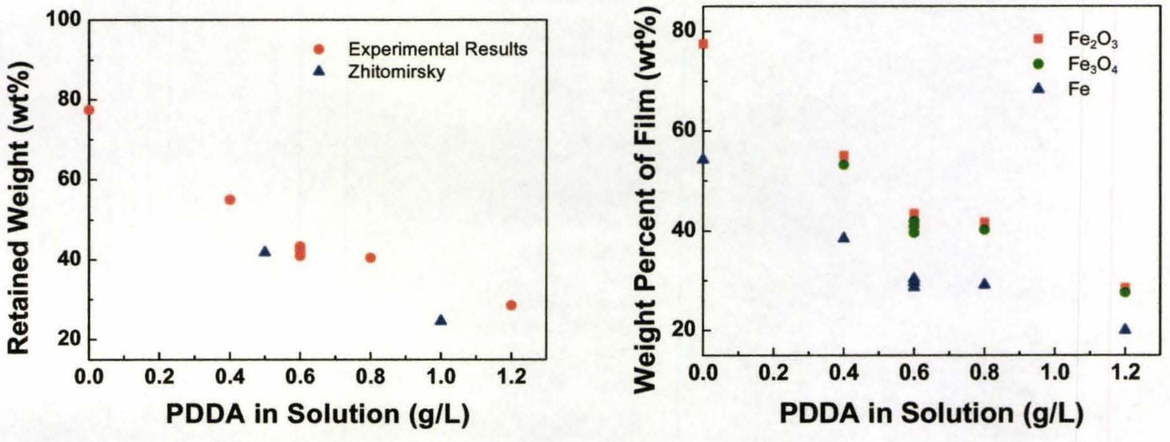

(a) (b)

Figure 5.2 (a) Experimental and literature (Zhitomirsky, 2003) values showing retained weight of films at 1200°C determined by TGA (b) Calculated haematite, magnetite and iron content.

Comparison of TGA data completed by Zhitomirsky (Zhitomirsky, 2003) showed similar retained weight values. The small differences in retained weight may be the result of different anode/cathode spacing. As electrolytic and electrophoretic deposition methods are influenced by anode/cathode spacing differently, any changes the electrode distancing can affect the iron oxide and polymer ratio within the deposit.

Table 5.1 Oxides and Iron compositions of Film

Sample	PDDA Solution Content (g/L)	Weight Retained at 1200°C (wt% as Fe_2O_3)	Fe_3O_4 (wt%)	Fe (wt%)
P1-6	0	77.53	74.95	54.23
P1-7	0.4	55.07	53.23	38.52
P1-8	0.6	42.36	40.95	29.63
P2-5	0.6	41.06	39.69	28.72
P2-6	0.6	43.48	42.03	30.41
P1-9	0.8	41.71	40.31	29.17
P1-10	1.2	28.61	27.66	20.01

Table 5.1 lists the calculated magnetite and iron weight content of the film. Results are plotted in Figure 5.2b. As the presence of maghemite cannot be eliminated, the actual iron oxide weight composition may be between the Fe_3O_4 and Fe_2O_3 value. Given the weight difference between the two oxides is small, calculations were done using the magnetite weight value.

5.4.2 Microscopy of Films

AFM shows a reasonably smooth film surface with a RMS of 5.695 nm. No special consideration in experimental procedure was taken to minimize surface roughness. For applications requiring a smoother surface, surface roughness can be reduced by using lower deposition currents and reducing the water to methanol ratio.

No measurable difference was found in film thickness between Samples P1-12 and P1-13. Samples P1-12 and P1-13 were made with PDDA solution concentrations of 0.6 and 0.8 g/L respectively. TGA showed only a 2 wt% difference between film polymer content at these deposited PDDA concentrations. Although small, this polymer content difference should be reflected in the film thickness.

HRTEM results (Figure 3.6) showed a very high density of nano-particles of iron oxide within the amorphous polymer matrix. As particles are approximately spherical, shape anisotropy was considered negligible. The particle spacing was extremely small and significant interparticle magnetic interaction can be assumed.

5.4.3 X-Ray Diffraction

Peak broadening was observed due to size of nano-particles. The one distinguishable peak matches with the major peak of both magnetite and maghemite. Slower scanning rates are required to obtain more useful results.

5.4.4 Superparamagnetic Criteria

Magnetic behaviour of all P1-Series samples within an applied field showed non-hysteresis behaviour above 20 K. Samples containing PDDA showed reasonable superimposition when the applied field was normalized by temperature (Figure 5.3). Therefore, by the criteria of superparamagnetism, the P1 Series with PDDA showed superparamagnetic properties.

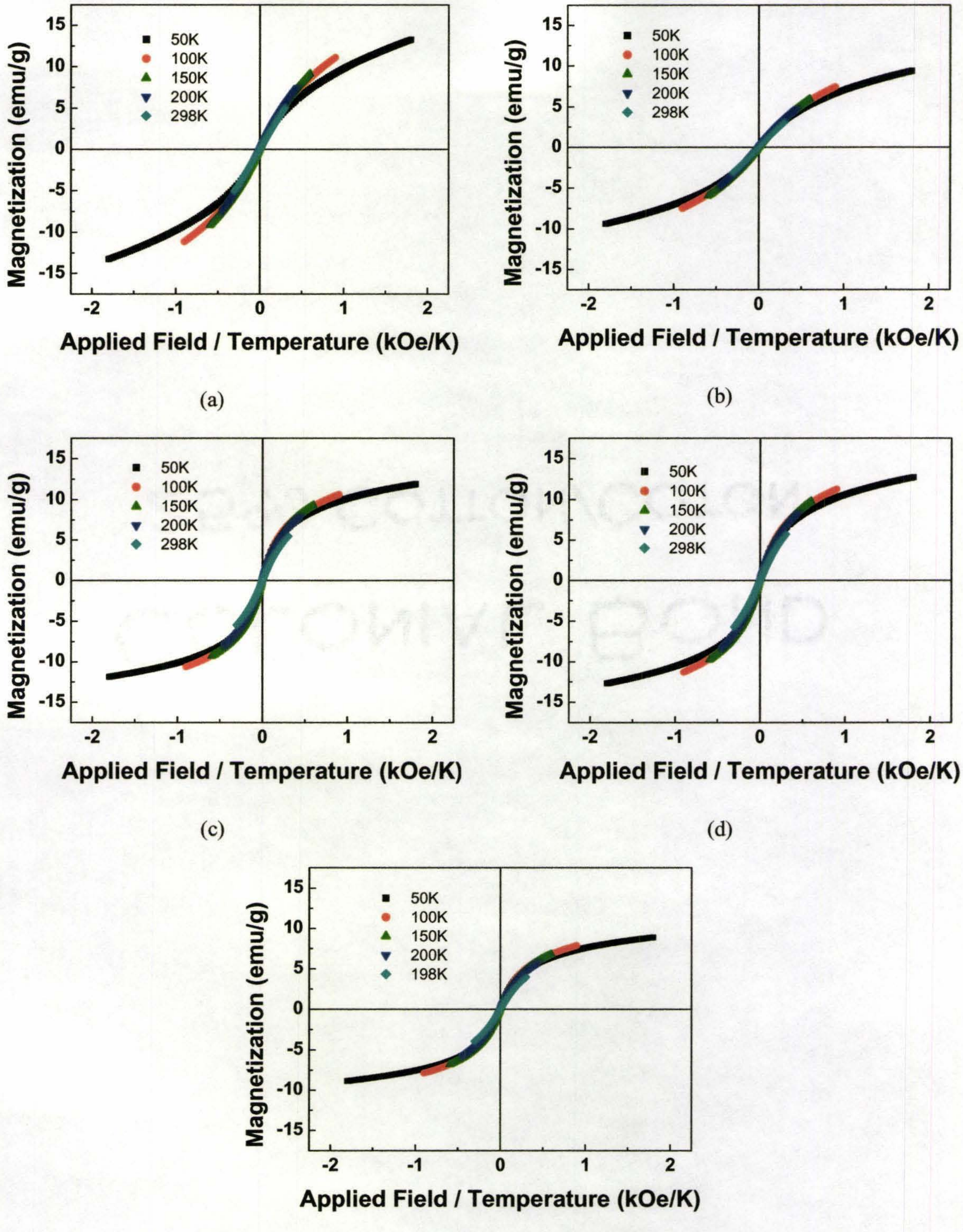

(a) (b) (c) (d) (e)

Figure 5.3 P1 Series with temperature normalized applied fields. (a) P1-1, no PDDA, (b) P1-2, 0.4 g/L PDDA, (c) P1-3, 0.6 g/L PDDA, (d) P1-4, 0.8g/L PDDA and (e) P1-5, 1.2 g/L PDDA.

However, the low initial susceptibility does not fit the anticipated behaviour of superparamagnetic nano-crystals of magnetite or maghemite. In the ideal case of sufficiently small, spherical magnetite (or maghemite) nano-particles, saturation magnetization should be reached at very low fields. The applied field has only to overcome the minutely small anisotropy energy and interaction energies in order to achieve saturation magnetization. Instead, composite samples from the the P1 Series showed a gradual increase in magnetization even at high fields. At room temperature the magnetization appears linear resembling paramagnetism except with higher orders of susceptibility.

P1 Series ZFC and FC results do show superparamagnetic behaviour above a blocking temperature. AC susceptibility measurements show relaxation phenomenon. This behaviour supports the existence of nano-particles but indicates the particles are not entirely, if at all, magnetite or maghemite. The measured saturation magnetizations of the P1 Series, taking into account the Fe_2O_3 weight content of the film, were less than a third the bulk saturation magnetization of maghemite. Including the loss expected due to the magnetic dead zone near the surface of the particle, this low saturation magnetization indicates that at least a portion of the particle is not an iron oxide and the particle may consist of an iron oxyhydroxide.

The P2 Series showed non-hysteresis magnetization behaviour, above a blocking temperature, when subjected to a magnetic field. Normalization of the applied field by temperature showed superimposition of the magnetization plot for both films with and without polymer (Figure 5.4). Films containing PDDA showed high initial susceptibility and magnetization plateaued at low fields. Saturation magnetization, once normalized by the iron oxide content and the magnetic dead zone incorporated, was comparable to bulk magnetite/maghemite and will be discussed later. ZFC and FC showed relaxation above the breaking temperature. Therefore, P2 Series composite samples exhibited superparamagnetic behaviour. Furthermore, superparamagnetic behaviour matches closely to nano-sized particles of magnetite/maghemite.

Sample P2-1 (no PDDA) showed similar behaviour to the P1 Series.

The superparamagnetic behaviour of films deposited without PDDA was unexpected and difficult to explain. One potential explanation is the existence of nano-sized iron oxide crystals within an iron hydroxide matrix. More work in analyzing the nature of the film would be necessary to produce a complete understanding of the observed magnetic properties.

5.4.5 Saturation Magnetizatoin

The three factors contributing with the saturation magnetization are (1) the iron oxide phase, (2) iron oxide content within the film and (3) the size of the iron oxide particles.

Saturation magnetization was calculated by extrapolating the magnetization versus applied field and taking the magnetization value at H = 0 as saturation. Magnetic behaviour, shown by the P1 Series, was similar to samples fabricated by Zhitomirsky (Zhitomirsky, 2003) using co-electrodeposition. Saturation magnetization of the

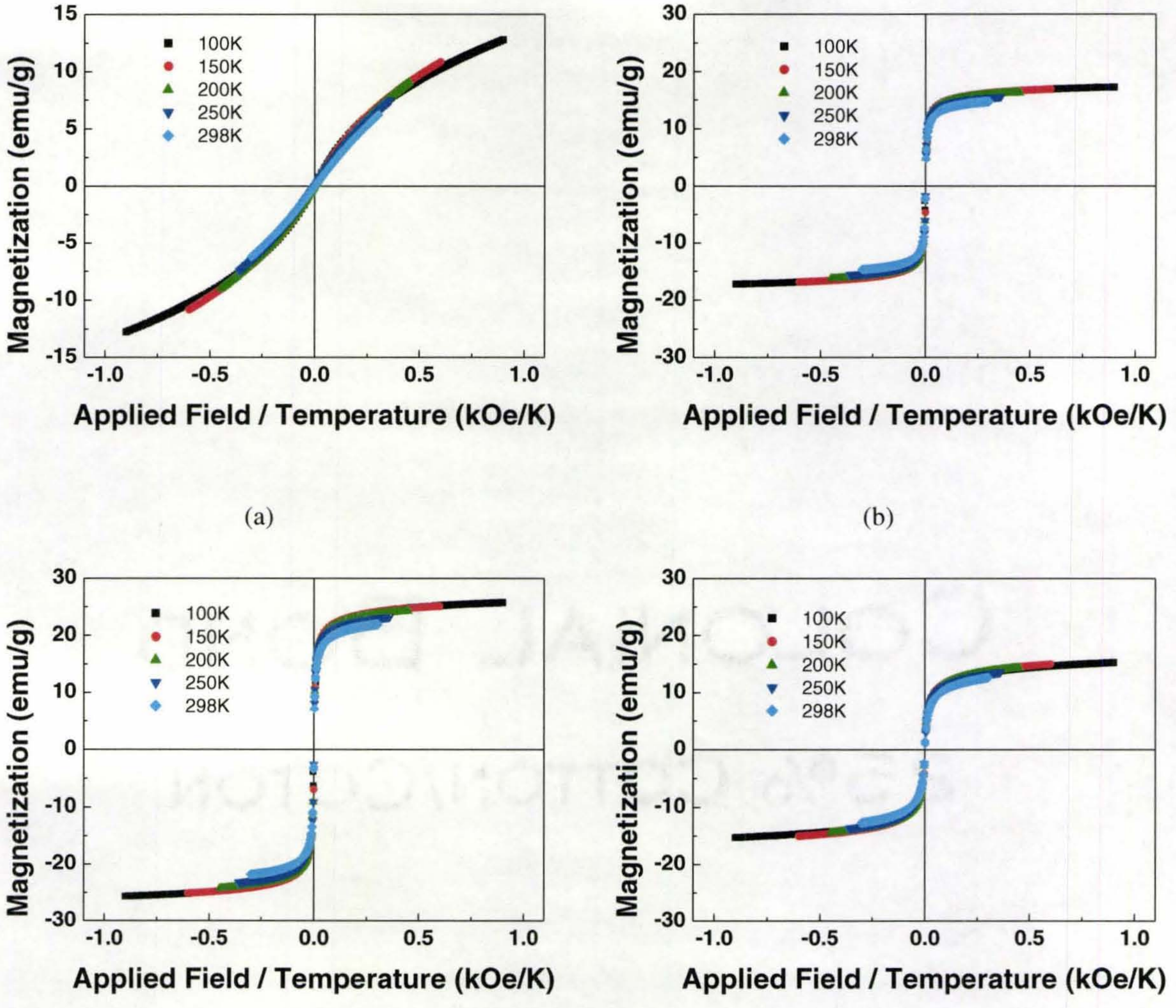

(a)

(b)

(c)

(d)

Figure 5.4 P2 Series with temperature normalized applied fields. (a) P2-1, no PDDA, (b) P2-2, 0.4 g/L PDDA, (c) P2-3, 0.6 g/L PDDA and (d) P2-4, 0.8g/L PDDA.

P1 Series decreased quickly at an inverse relationship with temperature (Figure 5.5a). Saturation magnetization at 2 K ranged between 6 and 10 emu/g which dropped to below 1.5 emu/g at room temperature.

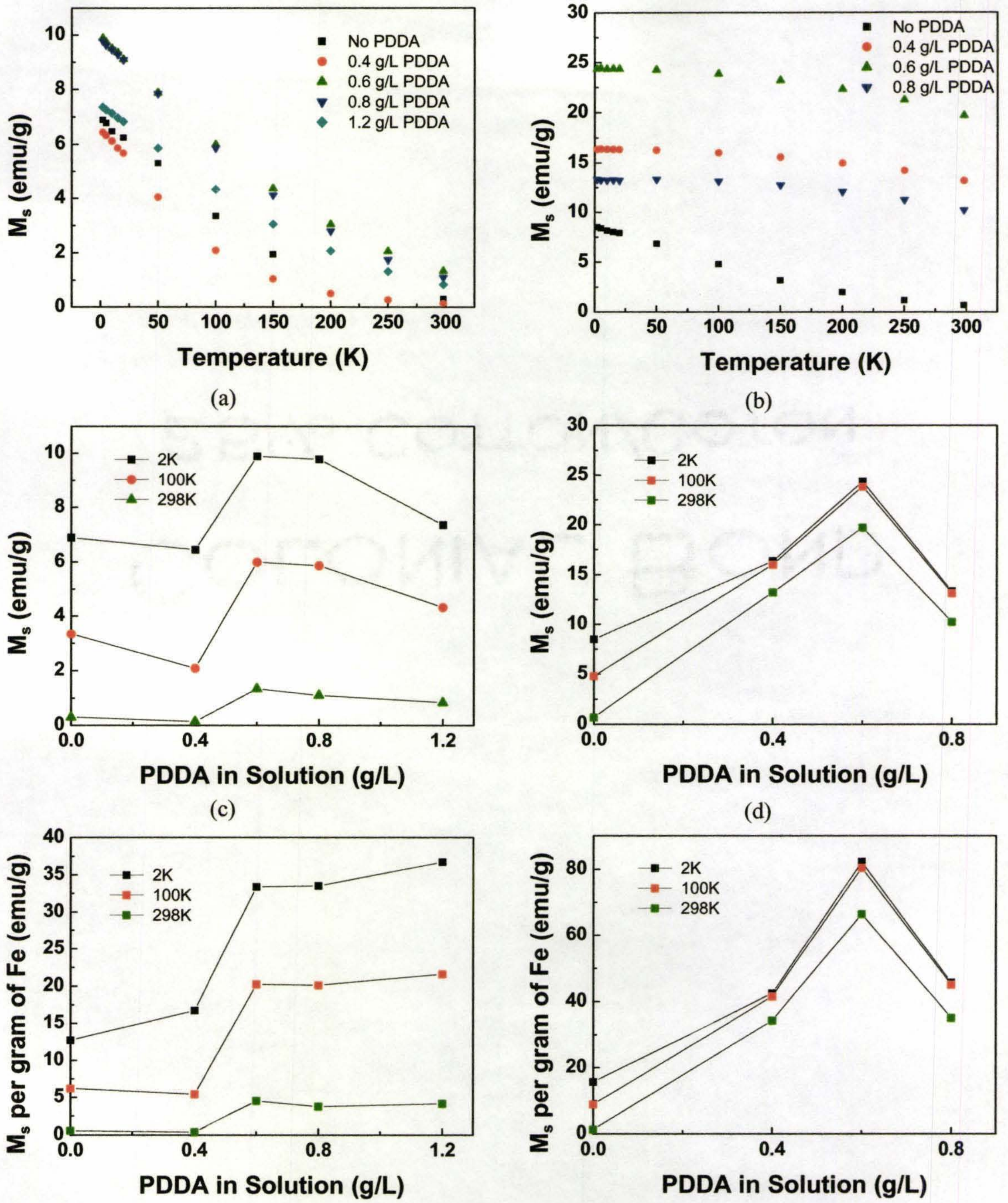

(a) (b)

(c) (d)

(e) (f)

Figure 5.5 (a) Saturation magnetization versus temperature for P1 Series, (b) saturation magnetization versus temperature for P2 Series, (c) saturation magnetization versus PDDA in solution for P1 Series, (d) saturation magnetization versus PDDA in solution for P2 Series, (e) saturation magnetization normalized by iron content versus PDDA in solution for P1 Series and (f) saturation magnetization normalized by iron content versus PDDA in solution for P2 Series.

The similar saturation magnetization behaviour of the P1 Series to the P1-1 and P2-1, both without polymer, may indicate these samples have similar iron phases. As samples P1-1 and P2-1 are thought to be a hydroxide phase, this raises the possibility that the P1 Series particles may also be an iron hydroxide.

Saturation magnetization of the P2 Series, shown in Figure 5.5b, were several factors higher than the P1 Series and less temperature sensitive within the tested temperature range. The P2-3 sample prepared with 0.6 g/L PDDA solution concentration showed the highest saturation magnetizations of 23.37 and 19.71 emu/g at 2 and 298 K respectively. Regression of the saturation magnetization with an increase in temperature followed the Bloch behaviour of $M_s \sim (1 - CT^{3/2})$ where C is a constant.

From both P1 and P2 Series, the films prepared with 0.6 g/L PDDA solution concentration showed the highest saturation magnetization (Figure 5.5c,d).

In order to isolate magnetic properties of the iron phases without the polymer, the saturation magnetization was normalized to the weight of iron and displayed in Figure 5.5e,f. The P1 Series showed very similar normalized saturation magnetizations for films prepared with 0.6 to 1.2 g/L PDDA. The P2 Series displayed a peak normalized saturation magnetization at 0.6 g/L PDDA.

5.4.6 Particle Size Calculations

Models by Godovsky (Godovsky, 1999) and Chantrell (Chantrell, 1978) were used to calculate particle size from magnetic measurements and TGA data. The Godovsky model, shown in equation 5.3, originally developed to use magnetization per unit volume, was modified to equation 5.4 for use of magnetization per unit weight. This eliminated the need for the polymer density which is unknown.

$$V = \frac{3X_{0,v}kT}{M_v^2}\frac{\rho_c}{\rho_m}\frac{c}{c+1} \tag{5.3}$$

where V is the particle volume, $X_{0,v}$ is the initial susceptibility by volume, M_v is the experimental saturation magnetizaton by volume, ρ_c is the density of the composite, ρ_m is the density of the magnetic material and 'c' is the weight fraction of magnetic material within the composite.

$$V = \frac{3X_0kT}{M^2}\frac{1}{\rho_m}\frac{c}{c+1} \tag{5.4}$$

where M is the bulk saturation magnetization by weight and X_0 is the bulk saturation magnetization by weight. This model is independent of bulk saturation values and, as long as the magnetic material is superparamagnetic, the exact identification of the iron oxide phase is not necessary. The model was developed for a composite material and therefore does not apply to samples P1-1 and P2-1 which were made without polymer. To check reliability of the model, calculations were done at 10, 100 and 298 K. Results are displayed in Table 5.2.

Table 5.2 Particle Size Calculated by Godovsky Model

Sample	**PDDA Concentration (g/L)**	**Calculated Particle Diameter (nm)**		
		10°K	100°K	298°K
P1-2	0.4	2.82	7.40	39.13
P1-3	0.6	2.99	4.90	11.61
P1-4	0.8	2.49	4.73	12.46
P1-5	1.2	2.59	4.65	12.22
P2-2	0.4	3.64	8.01	11.32
P2-3	0.6	2.93	6.45	9.12
P2-4	0.8	3.37	6.96	8.24

Results from the Godovsky model was shown to differ with temperature. Differences between obtained values using 10 and 298 K magnetic measurements vary by a multiple of three. The model should only provide the magnetic particle size of the magnetically effective component of the particle and the thickness of the magnetically dead zone must be added to the final particle size in order to compare with TEM results. The magnetically dead zone varies between 0.5 and 1 nm in thickness (Chantrell, 1978, Kim 2001; Prene, 1993; Dormman, 1996) and the addition of 1 to 2 nm to the particle diameter calculated at 10 K showed good correlation with TEM images.

Particle size calculation of sample P1-2 at 298 K showed an excessively large particle size. As this value would be well above the superparamagnetic critical size, this value cannot be valid. The hysteresis curve at 298 K showed the material to behave closer to paramagnetic than superparamagnetic, preventing the Godovsky model from accurately evaluating particle size.

The particle size, seen at all three temperatures, showed a decrease in particle size with an increase in polymer content within the P1 Series. With only three samples for the

P2 Series, it is difficult to determine any definite trend. Particle size calculated at room temperature showed a decrease in particle size with an increase in polymer but sizes calculated at 2 K show similar sizes.

The Chantrell model (equation 5.5) required the use of bulk saturation magnetization values and thus the state of the magnetic component must be known. This prevents the use of this model for the P1 Series. Also, P2-1 had no polymer and does not meet the criteria for the model.

H_0 was calculated by plotting magnetization versus 1/H from the high field magnetization data. The plot was extrapolated to zero magnetization and the x axis value is $1/H_0$. The particle size values obtained, from 298 K experimental data, for the P2 Series composite films are displayed in Table 5.3.

$$D_v = \left(\frac{18kT}{\pi M_{bulk}} \sqrt{\frac{X_0}{3cM_{bulk}H_o}} \right)^{1/3} \tag{5.5}$$

Table 5.3 Particle Size Calculated by Chantrell Model

Sample	PDDA Concentration (g/L)	Particle Diameter (nm)	Particle Volume (nm^3)
P2-2	0.4	4.46	46.43
P2-3	0.6	4.46	46.43
P2-4	0.8	3.42	20.93

The particle sizes obtained, once the magnetically dead zone was considered, matches well with TEM observations. Sample P2-4 showed a smaller particle size than the samples made with less polymer.

At nano-sizes, small differences between the non-relaxing particle diameters translates into large volumetric differences. Samples P2-2 and P2-3 had over twice the magnetically active volume per particle than Sample P2-4. This results in different anisotropy energy barriers, percentage of magnetic material near the surface of the particle (magnetically altered) and the particle density.

Assuming the iron oxide is in the magnetite phase and assuming the magnetically dead zone is 0.5 nm thick, the particle sizes obtained by the Chantrell model were used to calculate the percentage of magnetically effective magnetite, the saturation magnetization of the magnetically effective magnetite and the particle density. These results are presented in Table 5.4.

As the magnetic dead zone was treated as magnetically inactive, only a portion of the iron oxide contributed to the magnetic properties. This contributing portion was deemed magnetically effective. Due to Samples P2-2 and P2-3 having identically calculated particle size, both share the same magnetically effective magnetite values. Sample P2-4, having a smaller particle size, has a larger percentage of magnetite near the surface of the particle resulting in a lower percentage of magnetically contributing magnetite.

This partially explains Sample P2-4 having a lower saturation magnetization than Sample P2-3. Sample P2-4 contains slightly less iron oxide than Sample P2-3 (higher polymer content) and, of this iron oxide, a lower fraction magnetically contributed to the saturation magnetization.

Table 5.4 Magnetically Effective Magnetite, Effective Saturation and Particle Density

Sample	PDDA Concentration (g/L)	Effective Fe_3O_4 (wt %)	M_s of Effective Fe_3O_4 (emu/g)	# of Particles (g^{-1})
P2-2	0.4	54.50	45.60	1.21×10^{18}
P2-3	0.6	54.50	88.44	9.28×10^{17}
P2-4	0.8	46.32	54.50	1.74×10^{18}

The saturation magnetization of the magnetically effective magnetite was calculated by assuming the magnetically dead iron oxide and the polymer had no contribution to the saturation magnetization. Experimental saturation magnetizations were normalized to the weight percentage of non-relaxing, magnetically effective iron oxide within the film. This normalized saturation magnetization was termed *effective saturation magnetization.*

Results show that Sample P2-3, made with 0.6 g/L PDDA solution concentration, had an effective saturation magnetization within the bulk saturation magnetization range as magnetite. As no other iron oxide has such a high saturation magnetization, is strong evidence that the predominate iron oxide phase in Sample P2-3 was magnetite.

Sample P2-4 showed an effective saturation magnetization below magnetite bulk values. This may be from two reasons. Firstly, the magnetically dead zone has been shown to range from 0.5 to 1 nm in thickness. Although calculations were done using a thickness of 0.5 nm, this may be an under-approximation and the model is quite sensitive to the input thickness. Calculations for P2-4 using a dead zone thickness of 0.8nm gives an effective saturation magnetization of 80 emu/g, comparable to magnetite bulk values.

Secondly, the presence of maghemite in solid solution with magnetite cannot be ruled out. Maghemite has a lower saturation magnetization than magnetite. Magnetite particles consisting partially of maghemite would lower both the effective saturation magnetization and the experimental saturation magnetization of the film.

In the case of Sample P2-2, even using a dead zone thickness of 1 nm, the calculated effective saturation magnetization values do not approach that of bulk magnetite. It does not appear that Sample P2-2, made with 0.4 g/L PDDA, was magnetite and may be partially maghemite and/or an iron hydroxide. The presence of maghemite/iron hydroxide may be the result of either oxygen exposure during fabrication or the film containing insufficient polymer to prevent oxygen exposure to the iron oxide.

5.4.7 ZFC and FC Magnetization

No quantitative method was found in the literature to establish the breaking temperature. The breaking temperature for this work has been defined as the temperature at which the M_{ZFC} and M_{FC} are different by only 1% when divided by the average between the two magnetizations as per equation 5.6.

$$\frac{2(M_{FC} - M_{ZFC})}{M_{FC} + M_{ZFC}} = 1\% \tag{5.6}$$

Results of this method in determining the breaking temperature and the average blocking temperature are shown in Figure 5.6a,b.

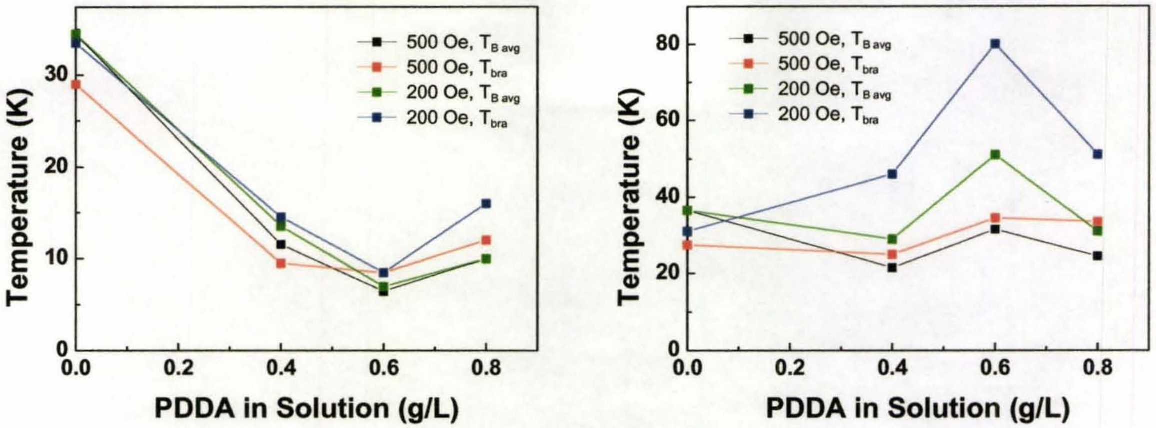

(a)

(b)

Figure 5.6 Blocking and breaking temperatures determined by ZFC and FC magnetic measurements. (a) P1 Series and (b) P2 Series.

Samples made without PDDA from both the P1 and P2 Series have similar DC magnetization characteristics. Their average blocking temperatures are similar within a few degrees, their magnetizations are within the same range and the characteristics of the plots are similar. This suggests, regardless of differences of deposition experimental procedures, Samples P1-1 and P2-1 films have similar iron phases.

Both Samples P1-1 and P2-1 (both without PDDA) and Sample P1-2 (0.4 g/L PDDA) showed breaking temperatures below their average blocking temperatures. Within a magnetite/maghemite, spherical, superparamagnetic nano-particle assembly, the breaking temperature represents the largest particle size within the particle distribution and having the highest individual particle blocking temperature, should always be higher than the average blocking temperature.

The P1 Series average blocking temperatures showed little sensitivity to the difference in 200 and 500 Oe fields, varying less than two degrees between the two fields. The average blocking temperature of P1 Series samples made with PDDA ranged from 6 to 13.5 K at these fields. As expected, the 200 Oe field always showed higher blocking temperatures than the 500 Oe field.

The P2 Series showed very different magnetic behaviour from the P1 Series. Whereas Sample P1-3, made with 0.6 g/L PDDA, showed the lowest blocking temperatures of the P1 Series, Sample P2-3 made with the sample polymer content showed the highest blocking temperatures of the P2 Series. P2 Series average blocking temperatures ranged from 21 to 51 K at the tested fields. Breaking temperatures ranged from 25 to 80 K. The P2 Series showed significantly more sensitivity to the difference in fields. Not enough data points exist to determine a trend within the blocking temperature.

P2 Series DC magnetization curves exhibit characteristics of high interparticle interactions. Differences between M_{ZFC} at $T_{B\ avg}$ and M_{FC} at 2 K are small and decrease with an increase in solution polymer concentration. Work done by Prené *et al* (Prené, 1993) observed a decrease between these magnetizations with a decrease in particle distancing and, thus, high interparticle interactions. Also consistent with Prené observations of high interparticle interaction is the near linear behaviour of both ZFC and FC curves above the blocking temperature seen in Samples P2-3 and P2-4.

At 500 Oe, breaking and average blocking temperatures varied by 3 degrees for Samples P2-2 and P2-3. Sample P2-4 showed a difference between the temperatures of 9 degrees. Small differences between the two temperatures have previously been used to describe a small particle size distribution, large particle interactions or both (Dormann, 1996; Prené, 1993). A small particle size distribution would lead to only small anisotropy differences between the average and maximum particle size, causing the average particle blocking temperature and the largest particle blocking temperature to be similar. In the case of large interparticle interaction, particles no longer act individually but as a collective causing only a small distribution in between blocking temperatures throughout the assembly.

5.4.8 AC Susceptibility

The temperature at which the maximum χ' occurs, T_{max}, is less than 10% greater than the true blocking temperature (Dormann, 1996). Therefore T_{max} can be used to approximate the blocking temperatures and used to describe blocking temperature behaviour.

As expected, T_{max} increased with an increase in frequency (decrease in provided relaxation time) as displayed in Figure 5.7a,b. The P1 Series showed little sensitivity in T_{max} between 10 and 10 000 Hz with only a few degrees change in T_{max}. The P2 Series T_{max} increased by 11 to 15 K when increasing the frequency from 10 to 10 000 Hz.

T_{max} values were significantly different between the two series as the P2 Series showed significantly higher T_{max} values than the P1 Series. T_{max} versus polymer concentration during depositions showed opposite trends between the two series and are displayed in Figure 5.7c,d. Films made with a PDDA solution concentration of 0.6 g/L displayed either the lowest or highest T_{max} for the P1 and P2 Series respectively. These

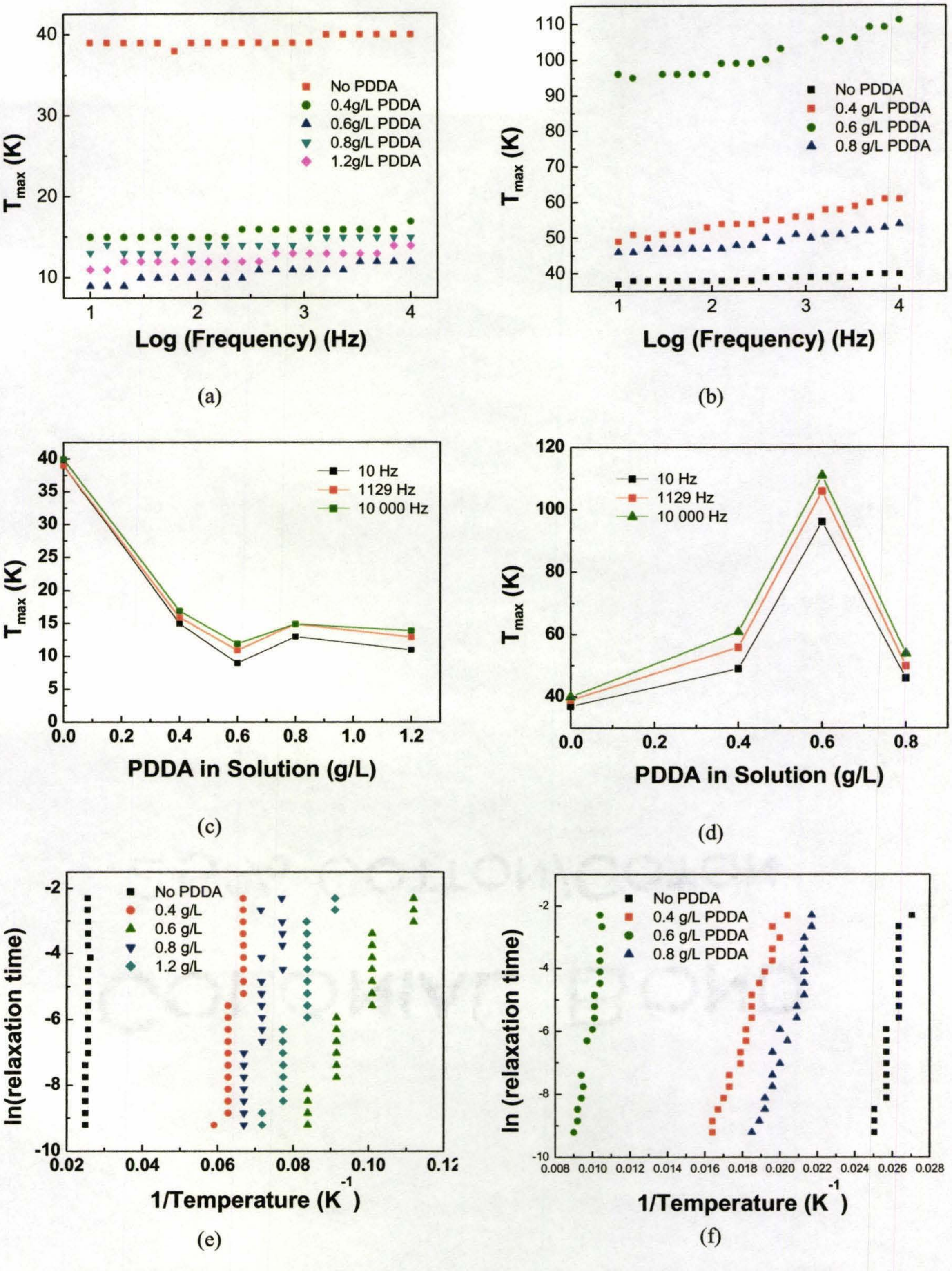

(a) (b)

(c) (d)

(e) (f)

Figure 5.7 (a) T_{max} verus Log(frequency) for P1 Series, (b) T_{max} verus Log(frequency) for P2 Series, (c) T_{max} versus PDDA solution concentration for P1 Series, (d) T_{max} versus PDDA solution concentration for Pd Series, (e) $\ln(\tau)$ verus $1/T_{max}$ for P1 Series and $\ln(\tau)$ verus $1/T_{max}$ for P2 Series.

differences in magnetic behaviour indicates that the iron oxide consists of different phases between the P1 and P2 Series.

5.4.9 Standard Relaxation Constant and Energy Barrier Calculations

Figure 5.7e,f shows the plot of ln(τ) versus 1/T_{max} from AC susceptibility measurements. The plot matched well with the Néel equation (modified using the effective energy barrier term, equation 5.7) showing an exponential increase in T_{max} with an increase in frequency.

$$\tau = \tau_0 \exp\left(\frac{E_{Beff}}{kT}\right) \tag{5.7}$$

Values obtained for τ_0 and $E_{B\,eff}$ from best fit curves are displayed in Table 5.5. Effective energy barriers are within the kT range as expected by superparamagnetic criteria of the thermal, above the blocking temperature, being greater than the magnetic reversal energy barrier. Obtained values of standard relaxation constants are well below the expected values of 10^{-9} to 10^{-12} seconds shown throughout literature (Dormann, 1996; Leslie-Pelecky, 1996; Kneller, 1966; Prené, 1993). However, work done by Kim (Kim,2001) on Fe_3O_4 nano-composite particles obtained experimental standard relaxation constant values of τ_0 = 7.8 x 10^{-24} seconds. Kim explained the difference from the physical model by the effects of interparticle interaction.

Standard relaxation values for the P1 Series vary significantly by many orders of magnitude. Effective magnetic reversal energy barriers of P1 Series containing polymer vary by one order of magnitude. These differences indicate a variance in iron phase within the P1 Series. The unknown phase(s) of the P1 Series prevents further interpretation of these results.

Table 5.5 Calculated relaxation constant and energy barrier

Sample	PDDA Concentration (g/L)	τ_0 (sec)	$E_{B\,eff}$ (J/m^3)
P1-1	0	3.30×10^{-50}	5.85×10^{-20}
P1-2	0.4	2.28×10^{-25}	1.09×10^{-20}
P1-3	0.6	1.79×10^{-12}	3.05×10^{-21}
P1-4	0.8	1.03×10^{-17}	6.45×10^{-21}
P1-5	1.2	2.84×10^{-16}	5.12×10^{-21}
P2-1	0	3.45×10^{-44}	5.02×10^{-20}
P2-2	0.4	2.73×10^{-17}	2.44×10^{-20}
P2-3	0.6	3.91×10^{-21}	5.75×10^{-20}
P2-4	0.8	2.69×10^{-21}	2.82×10^{-20}

Samples P1-1 and P2-1, both made without polymer, have similar energy barriers. Due to the small change in T_{max} throughout the tested frequency range, large error can be expected for obtained τ_0 values. Samples P1-1 and P2-1 show similar $\ln(\tau)$ intercepts of -113.94 and -100.08 respectively but, due to the exponential relation, the difference between the two intercepts translates into large differences in calculated τ_0 values. Also, equation 5.7 is a simplification of a very complex system and error can be associated with values obtained by the use of this equation. Therefore the differences of τ_0 values between P1-1 and P2-1 are not large enough to indicate them being of different magnetic materials. Similar effective energy barriers combined with similar DC magnetization behaviour and saturation magnetization does support the magnetic components of P1-1 and P2-1 are of like states.

Values obtained from the P2 Series were of closer consistency than the first series. Samples P2-2 and P2-4 displayed similar energy barriers with a difference between τ_0 values of four orders of magnitude. Samples P2-3 and P2-4 had similar τ_0 values but P2-3 had a higher energy barrier.

Differences in energy barriers can be the result of three factors. Firstly, any differences between iron oxide phases will lead to differences in energy barriers. Secondly, differences in particle sizes will lead to differences in anisotropy energy contributing to the energy barrier. Thirdly, differences in particle spacing, especially at such high densities, will influence interparticle interaction component of the effective magnetic energy barrier.

Sample P2-3 having an energy barrier twice as high as Sample P2-2 can only be explained using two of these factors. Sample P2-3, made with a higher polymer solution concentration than Sample P2-2, was expected to have equal or smaller particle sizes than Sample P2-2. However, particle size calculations shows similar particle sizes and, if Sample P2-3 did contain a smaller particle size than Sample P2-2, this would only reduce the energy barrier for Sample P2-3 below Sample P2-2 due to a smaller anisotropy contribution. Therefore Sample P2-3's higher energy barrier must be explained by a phase difference and/or interparticle interaction. As iron oxide is much more dense than PDDA, the difference of 13 wt% retained from TGA between the two samples leads to large differences in particle spacing. With the relation of $1/d^3$ for interparticle interaction, P2-3 is expected to have higher particle-particle interaction, increasing the magnetic reversal energy barrier when compared to P2-2. Also, as indicated by the calculated effective saturation magnetizations, the iron oxide phase in Samples P2-2 and P2-3 are believed to be predominately maghemite/iron hydroxide and magnetite respectively. Differences in anisotropy constants between these two phases, at such particle sizes, are expected to be within the same order of magnitude ($\sim 10^5$ J/m^3) but will contribute to the energy barrier difference. Differences in iron phases would also explain differences in τ_0 values.

Differences between the energy barriers of Samples P2-3 and P2-4 are predominately from a difference in particle size. Calculations show Sample P2-4 to have half the non-relaxing volume per particle as Sample P2-3. Due to the anisotropy relation given in equation 1.4, the anisotropy energy barrier of Sample P2-4 should be half of Sample P2-3. Other factors which must be included is the possibility of phase and interparticle interaction differences. Effective saturation magnetization calculations present the possibility that Sample P2-4 consists partially of maghemite whereas Sample P2-3 exists entirely as magnetite. Also, as Samples P2-3 and P2-4 have similar iron oxide content, differing only by 2%, Sample P2-4 having a smaller particle size contains a higher particle density within the polymer matrix. Calculations (shown in Table 5.4) show Sample P2-4 to have twice the particle density than Sample P2-3, meaning closer particle spacing, an increase in nearest neighbors and higher interparticle interaction.

5.4.10 Electrodeposition of Nano-Composite Film using PDDA as Polymer Matrix

The co-electrodeposition process has been shown to successfully fabricate iron oxide/polymer nano-composite, superparamagnetic films. The iron oxide states are composed of magnetite and possibly maghemite. TEM observations and TGA show the films to be a high density of magnetic particles with small spacing, in some cases being less than 1 nm. Particles were observed as being spherical. P1 Series which also showed superparamagnetic behaviour but inconsistent with magnetite and maghemite. The P1 Series may consist of an iron oxyhydride.

Films deposited without polymer were of similar iron phases even with differences in P1 and P2 Series experimental procedure. Samples P1-1 and P2-1 showed similar magnetic properties indicating the films to have contained the same iron phases. Both showed similar saturation magnetizatons, effective energy barriers, DC magnetization behaviour and blocking temperatures (from both DC and AC measurements). Films are believed to be an iron oxyhydroxide, potentially with random, crystalline grains within an amorphous matrix.

The concentration of polymer was shown to have a direct relation to the iron oxide to polymer composition within the deposited film. An increase in PDDA concentration of the solutions increased the polymer content within the film as shown by TGA. Particle size calculations by the Godovsky model showed that an increase in polymer concentration reduced the deposited particle size.

The depositing conditions used for the P1 Series failed to deposit consistent magnetite/maghemite nano-particles. The P1 Series showed inferior magnetic properties to iron oxides and magnetic material suspected of being partially iron hydroxide. Magnetic properties of P1 Series varied significantly indicating the iron phase my not be consistent throughout series. Failure to deposit iron oxides was attributed to experimental procedure using an inadequate forming gas flow rate to provide the required reducing environment and/or incomplete draining of solution from vessel creating a humid drying environment.

Deposition conditions of the P2 Series was successful in depositing magnetite nano-particles. Sample P2-3 exhibited an effective saturation magnetization possible only by the magnetic phase existing predominately as magnetite. Sample P2-4 displayed magnetic properties suggesting a portion of the iron oxide being maghemite with the remainder being magnetite. This may be the result of oxygen exposure during deposition.

Deposition with a polymer solution concentration of 0.4 g/L, using the P2 Series experimental procedure, did not successfully obtain magnetite nano-particles. Sample P2-2 exhibited an effective saturation magnetization well below bulk values of magnetite. TGA showed a polymer to iron oxide ratio of 0.82 which was significantly lower than the 1.38 ratio from Sample P2-3 proven to maintain magnetite. Therefore, films deposited with 0.4 g/L PDDA solution concentrations may not contain enough polymer to act as an oxygen barrier and prevent the oxidation of magnetite.

CHAPTER 6

CONCLUSIONS

Experiments were conducted to better understand fabrication and magnetic properties of superparamagnetic, iron oxide/polymer nano-composite thin films, produced by a combined electrolytic and electrophoretic deposition process. Iron chloride salts were used to provide an iron ion within a methanol/water/polymer solution. Deposition and drying of the deposit was done under a reducing environment. The apparatus used was designed and constructed to meet the experimental requirements of this work.

Deposited films were characterized using TGA, SEM, AFM, TEM and XRD. Magnetic characterization of the material was done by measurements of magnetization versus applied field, ZFC, FC and AC susceptibility measurements. Magnetic measurements were done in a temperature range of 2 to 298 K.

Experiments were conducted using PDDA, PAM-PDDA and PEI polymers as the matrix material. PAM-PDDA composites displayed low adhesion at all water/methanol solutions used. Adhesion of PEI composites ranged from poor to acceptable with an increase from 0.4 to 0.8 g/L PEI solution concentration. However, composites made with 0.8 g/L PEI solution concentration show no indication of strong magnetic properties. Therefore, PAM-PDDA and PEI polymers were considered inferior to PDDA which has been shown to have good adhesion and magnetic properties at all polymer concentrations tested.

Deposited films, using PDDA as the matrix polymer, showed a low roughness. Film thickness of samples deposited with 0.4 and 0.6 g/L PDDA solution concentration for 3 minutes were measured as 1.5 μm. HREM images showed the film to contain spherical, crystalline nano-particles of iron oxide within an amorphous, polymer matrix. Crystallographic orientation of particles appeared random. Film showed high volumetric density of particles within matrix. Particle spacing was very small and observed to be less than 1 nm.

The co-electrodeposition process, using PDDA as the polymer matrix, has been shown to successfully fabricate iron oxide/polymer nano-composite, superparamagnetic thin films. Deposition solution concentration of PDDA was shown to have a direct relation to the magnetic properties of the deposited film. An increase in polymer concentration within the solution decreased the iron oxide to polymer ratio within the deposited film. Particle size calculations indicated an increase in polymer concentration reduced the deposited particle size.

Optimum deposition conditions and polymer concentrations have been shown to produce isolated magnetite particles within the superparamagnetic size range. Sample P2-3, made with a solution concentration of 0.6 g/L PDDA from the P2 experimental procedure, has been shown to contain predominately magnetite. Sample P2-3, containing an iron oxide to polymer ratio of 1.38, exhibited the highest saturation magnetization of 19.71 emu/g at 298°K from the series. Sample P2-4, made with a higher polymer concentration of 0.8 g/L PDDA, displayed a lower saturation magnetization of 10.25 emu/g at 298 K.

A minimum polymer content was required to preserve the magnetite phase. Sample produced with 0.4 g/L PDDA, containing an iron oxide to polymer ratio of 0.82, contained an inadequate amount of polymer to maintain magnetite from oxidation.

Particle size was calculated by the Godovsky and Chantrell models. The Godovsky model was sensitive to the temperature as calculated particle size varied at different temperatures. Particle sizes obtained at 2 K matched well with TEM measurements. The Chantrell model was valid only for the P2 Series and calculated sizes were in good agreement with TEM measurements. Particle size varied with polymer concentration and ranged within the order of 4 to 5 nm in diameter. Effective saturation magnetization values were calculated using TGA and particle sizes obtained from the Chantrell model.

Particle size differences resulting in the ratio of iron oxide within the magnetically dead zone, was partially attributed to the difference between saturation magnetization values between samples made with 0.6 and 0.8 g/L PDDA from the P2 Series.

ZFC and FC show relaxation consistent with superparamagnetic behaviour. The highest blocking temperature, determined by ZFC, was 51 K at 200 Oe from Sample P2-3 (made with 0.6 g/L PDDA). Blocking temperatures of the P2 Series ranging from 21 to 51 K at fields 200 and 500 Oe. ZFC and FC curves displayed characteristics of high interparticle interaction.

Sample P2-3 showed the highest T_{max} temperatures from AC susceptibility measurements, increasing from 96 to 111 K at frequencies of 10 to 10 000 Hz respectively. AC susceptibility data was used to calculate standard relaxation constants and magnetic reversal energy barriers. Standard relaxation constant values were well below values expected from the physical model and discrepancies have been attributed to high magnetic interparticle interaction. Differences in AC susceptibility results and magnetic reversal energy barriers have been attributed to differences in iron state, particle-particle spacing (interparticle interaction) and particle size.

The experimental procedure used to fabricate the P1 Series failed to produce consistent iron oxide nano-particles. Although magnetic properties of composite films were superparamagnetic, saturation magnetization values were well below iron oxide strengths. Saturation magnetization varied with polymer concentration but always below 3 emu/g at 298°K. Extreme variance in magnetic properties, calculated relaxation constants and magnetic reversal energy barriers indicated inconsistency in iron phases and/or composition. Particles may have consisted partially as iron hydroxide. As the P2 Series successfully deposited iron oxide nano-particles, the iron phase of the deposited particles have been shown to be sensitive to the deposition reducing environment and drying conditions.

Films deposited without polymer were of similar iron states regardless of differences between P1 and P2 Series experimental procedure. Samples P1-1 and P2-1 showed similar saturation magnetizatons, effective energy barriers, DC magnetization behaviour and blocking temperatures (from both DC and AC measurements), indicating similar iron states. Films are believed to be an iron hydroxide which may consist of isolated crystalline grains within an amorphous matrix.

An intermediate step to the co-electrodeposition process has been proposed, specific to this deposition. The magnetite formation may occur far enough away from the cathode to require further transport. As magnetite has a negative zeta potential within its stable pH range and would be electrostatically repulsed from the cathode, the positively charged polymer must combine with the magnetite particle and provide an overall positive zeta potential to the complex. Transport to the cathode would then occur via electrophoresis and final deposition would occur by coagulation at the cathode.

REFERENCES

Brown, F.W., "Magnetostatic Principles in Ferromagnetism". North-Holland Publishing Company. New York, 1962.

Callister, W.D., Materials Science and Engineering: An Introduction. 6th Edition, John Wiley & Sons, Inc., US, 2003.

Chantrell, R.W., Ayob, N.Y. and Popplewell, J., "The Low Field Susceptibility of a Textured Superparamagnetic System". *J. Mag. Mag. Mat.* 53 (1985) 199.

Chantrell, R.W., Popplewell, J. and Charles, S.W., "Measurements of Particle Size Distribution Parameters in Ferrofluids". *IEEE Trans. Mag.* Mag-14 (1978) 975.

Chantrell, R.W. and Wohlfarth, E.P., "Dynamic And Static Properties of Interacting Fine Ferromagnetic Particles". *J. Mag. Mag. Mat.* 40 (1983) 1.

Cornell, R.M. and Schwertmann, U., The Iron Oxides. SCH, New York, 1996.

Dormann, J.L., "Effect of interparticle interactions on the dynamical properties of γ-Fe_2O_3 nanoparticles". *J. Mag. Mag. Mat.* 183 (1998) L255.

Dormann, J.L. *et al.*, "From pure superparamagnetic regime to glass collective state of magnetic moments in γ-Fe_2O_3 nanoparticle assemblies". *J. Mag. Mag. Mat.* 187 (1997) L139.

Dormann, J.L., Fiorani, D. and Tronc, E., "Magnetic Relaxation in Fine-Particle Systems". *Advances in Chemical Physics.* 98 (1997) 283.

Dormann, J.L *et al*, "Thermal variation of the relaxation time of the magnetic moment of γ-Fe_2O_3 nonparticles with interparticle interactions of various strengths". *Phys. Rev. B.* 53 (1996) 14291.

El-Hilo, M., O'Grady, K. and Chantrell, R.W., "Susceptibility Phenomena in a Fine Particle System". *J. Mag. Mag. Mat.* 114 (1992) 307.

Iida, S. *et al*, "Details of the Electronic Superstructure of Fe_3O_4". *J. Appl. Phys.* 53 (1982) 2164.

Kim, D.K. *et al.* "Synthesis and Characterization of Surfactant-Coated Superparamagnetic Monodispersed Iron Oxide Nanoparticles". *J. Mag Mag Mats.* 225 (2001) 30.

Kittel, C., "Theory of the Structure of Ferromagnetic Domains in Films and Small Particles". *Phys. Rev.* 70 (1946) 965.

Kittel, C., "Physical Theory of Ferromagnetic Domains". *Rev. Mod. Phys.* 21 (1949) 541.

Kneller, E. and Wohlfarth, E.P., "Effect of Thermal Fluctuations on the Anhysteretic Process in Ferromagnetic Fine-Particle Assemblies". *J. Appl. Phys.* 37 (1966) 4816.

Kroll, E.C., Synethesis and Characterization of Superparamagnetic Iron Oxide-Alginate Hydrogels and Fluid. McMaster, 1996.

Kuhn, A.T. and Chan, C.Y., "pH Changes at Near-Electrode Surfaces". *J. App. Electrochemistry.* 13 (1983) 189.

Leslie-Pelecky, D.L. and Rieke, R.D., "Magnetic Properties of Nanostructured Materials" *Chem. Mater.* 8 (1996) 1770

Néel, L., "Some Theoretical Aspects of Rock-Magnetism". *Adv. Phys.* 4 (1955) 191.

Néel, L., C.R. Acad. Sci. 228 (1949) 664.

Ovchinnikova, T.M. and Rotinyan, A.L., "Acidity Measurements in the Layer Adjacent to the Cathode by Means of a Glass Electrode". *Russian Journal of Physical Chemistry.* 37 (1963) 228.

Prene, P. et al, "Magnetic Properties of Isolated γ-Fe2O3 Particles". *IEEE Trans. Mag.* 29 (1993) 2658.

Sarkar, P. and Nicholson, P.S., "Electrophoretic Deposition (EPD): Mechanisms, Kinetics, and Applications to Ceramics". *J. Am. Ceram. Soc.* 79 (1996) 1987.

Shchukin, D.G. *et al.* "Synthesis of nanosized Magnetic Ferrite Particles Inside Hollow Polyelectrolyte Capsules". *J. Phys. Chem. B.* 107 (2003) 86.

Slizhis, R.P., *Galvanotechnik.* 61 (1970) 653.

Smith, W.F., Foundations of Materials Science and Engineering, 2nd Edition, McGraw-Hill, Inc., Toronto, 1993.

Standley, K. J., Oxide Magnetic Ceramics. Clarendon Press, New York, 1972.

Tari, A., Popplewell, J. and S.W. Charles. "Observation of Spin Glass Behaviour in Ferrofluids". J. Mag. Mag. Mat. 15-18 (1980) 1125.

Ulberg, Z.R. and Deinega, Y.F., Electrophoretic Composite Coatings. Ellis Horwood, Toronto, 1992.

Valenzuela, R., Magnetic Ceramics. Cambridge University Press, New York, 1994

Van der Biest, O.O. and Vandeperre, L.L. "Electrophoretic Deposition of Materials". *Annu. Rev. Mater. Sci.* 29 (1999) 327.

Zhitomirsky, I., "New Developments in Electrolytic Deposition of Ceramic Films". *Am. Ceram. Soc. Bull.*. (2000) 57.

Zhitomirsky, I., "Cathodic Electrodeposition of Ceramic and Organoceramic Materials. Fundamental Aspects". *Advances in Colloid and Interface Science.* 97 (2002) 279.

Zhitomirsky, I. and Petric, A., "Electrolytic and electrophoretic deposition of CeO_2 films". *Materials Letters.* 40 (1999) 263.

Zhitomirsky, I. and Petric, A., "Electrochemical deposition of yttrium oxide". *J. Mat. Chem.* 10 (2000) 1215.

Zhitomirsky, I. and Petric, A., "Electrolytic deposition of zerconia and zirconia inorganocermaic composites". *Materials Letters.* 46 (2000) 1.

Zhitomirsky, I. and Petric, A., "Electrochemical deposition of ceria and doped ceria filma". *Ceramics International.* 27 (2001) 149.

I. Zhitomirsky, M. Niewczas, A. Petric. "Electrodeposition of hybdrid organic-inorgranic films containing iron oxide". *Materials Letters.* 57 (2003) 1045.